Puncture initial data for black-hole binaries with high spins and high boosts

Ian Ruchlin,[1,2] James Healy,[2] Carlos O. Lousto,[2] and Yosef Zlochower[2]

[1]*Department of Mathematics, West Virginia University, Morgantown, West Virginia 26506, USA*
[2]*Center for Computational Relativity and Gravitation, School of Mathematical Sciences, Rochester Institute of Technology, 85 Lomb Memorial Drive, Rochester, New York 14623, USA*

(Received 30 October 2014; revised manuscript received 2 November 2016; published 27 January 2017)

We solve the Hamiltonian and momentum constraints of general relativity for two black holes with nearly extremal spins and relativistic boosts in the puncture formalism. We use a non-conformally-flat ansatz with an attenuated superposition of two Lorentz-boosted, conformally Kerr or conformally Schwarzschild 3-metrics and their corresponding extrinsic curvatures. We compare evolutions of these data with the standard Bowen-York conformally flat ansatz (technically limited to intrinsic spins $\chi = S/M_{\rm ADM}^2 = 0.928$ and boosts $P/M_{\rm ADM} = 0.897$), finding, typically, an order of magnitude smaller burst of spurious radiation and agreement with inspiral and merger. As a first case study, we evolve two equal-mass black holes from rest with an initial separation of $d = 12M$ and spins $\chi_i = S_i/m_i^2 = 0.99$, compute the waveforms produced by the collision, the energy and angular momentum radiated, and the recoil of the final remnant black hole. We find that the black-hole trajectories curve at close separations, leading to the radiation of angular momentum. We also study orbiting nonspinning and moderate-spin black-hole binaries and compare these with standard Bowen-York data. We find a substantial reduction in the nonphysical initial burst of radiation which leads to cleaner waveforms. Finally, we study the case of orbiting binary black-hole systems with spin magnitude $\chi_i = 0.95$ in an aligned configuration and compare waveform and final remnant results with those of the SXS Collaboration [A. H. Mroue *et al.*, Phys. Rev. Lett. **111**, 241104 (2013).], finding excellent agreement. This represents the first moving puncture evolution of orbiting and spinning black holes exceeding the Bowen-York limit. Finally, we study different choices of the initial lapse and lapse evolution equation in the moving puncture approach to improve the accuracy and efficiency of the simulations.

DOI: 10.1103/PhysRevD.95.024033

I. INTRODUCTION

The detection of gravitational waves from merging binary black holes [1,2], as predicted by numerical relativity simulations [3–5], further highlights that general relativity is central to the modern understanding of much of astrophysics, from cosmological evolutions down to the end state of large stars. Crucial to this is the correctness of the theory itself and the elucidation of its predictions [6,7]. While much can be done using analytic techniques, one of the most interesting regimes—the merger phase of compact-object binaries—requires the use of large-scale numerical relativity simulations [8,9]. In order to evolve these systems, one requires appropriate initial data that allow for the simulation of binaries with astrophysically realistic parameters. Perhaps most important and challenging of all is the inclusion of large spins.

Highly spinning black holes (BHs) are thought to be common. For example, supermassive BHs with high intrinsic spins are fundamental to the contemporary understanding of active galaxies and galactic evolution, in general. In units with $c = 1$ and $G = 1$, a BH's spin magnitude S (i.e., intrinsic angular momentum) is bounded by its mass m, where the maximum dimensionless spin is given by $\chi \equiv S/m^2 = 1$. While it is actually hard to have an accurate measure of astrophysical BH spins, in a few cases the spins have been measured [10] and some were found to be near the maximal value. Since galactic mergers are expected to lead to mergers of highly spinning BHs, it is important to be able to simulate black-hole binaries (BHBs) with high spins in order to model the dynamics of these ubiquitous objects.

Spin can greatly affect the dynamics of merging BHBs. Important spin-based effects include the *hang-up* mechanism [11], which delays or prompts the merger of the binary according to the sign of the spin-orbit coupling; the *flip-flop* of spins [12], which is due to a spin-spin coupling effect capable of completely reversing the sign of individual spins; and finally, highly spinning binaries may recoil at thousands of km/s [13,14] due to the asymmetrical emission of gravitational radiation induced by the BH spins [15,16]. These effects are maximized for highly spinning BHs.

As a consequence of spin-orbit and spin-spin interactions, high spins can have a dramatic effect on the gravitational waveform. For example, unlike low-spin binaries, highly spinning binaries can radiate more than 11% of their rest mass [17,18], the majority of which emanates during the last moments of merger, down to the formation of a final single spinning BH. Efforts to interpret

gravitational wave signals from such systems require accurate model gravitational waveforms [19–23].

The *moving puncture approach* [4,5] has proven to be very effective in evolving BHBs with similar masses and relatively small initial separations, as well as small mass ratios [24] and large separations [25]. It is also effective for more general multiple BH systems [26], hybrid BH–neutron-star binaries [27], and gravitational collapse [28]. However, numerical simulations of highly spinning BHs have proven to be very challenging. The most commonly used initial data to evolve those binaries, which are based on the Bowen-York (BY) ansatz [29], use a conformally flat 3-metric. This method has a fundamental spin upper limit of $\chi = 0.928$ [30,31]. Even when relaxing the BY ansatz (while retaining conformal flatness), the spin is still bounded above by $\chi = 0.932$ [32].

In order to exceed this limit and approach maximally spinning BHs with $\chi = 1$, one has to allow for a more general 3-metric that captures the non-conformally-flat aspects of the Kerr geometry. Dain showed [33] that it is possible to find solutions to the initial value problem representing a pair of Kerr-like BHs. This proposal was implemented for the case of thin-sandwich initial data [34–36] with excision of the BH interiors, and produces stable evolutions of orbiting BHBs with $\chi \sim 0.97$ [17,37], and more recently $\chi \sim 0.998$ [38,39]. Dain's method was also tested for the case of head-on collisions (from rest) of spinning BHs using the moving puncture approach, which does not employ excision. These are compared to the BY data with spins up to $\chi = 0.90$ [40].

In this paper we revisit, and numerically implement, the problem of finding solutions to the puncture initial value problem representing two nearly-extremal-spin BHs, and the subsequent evolution using the moving puncture approach—the most widespread method to evolve BHBs, implemented in the open source EinsteinToolkit [41–44].

To solve for these new data, we construct a superposition of two conformally Kerr 3-metrics with the corresponding superposition of Kerr extrinsic curvatures. Note that we do not use the Kerr-Schild slice [45], but rather use the Boyer-Lindquist slice, which is amenable for puncture evolution. To regularize the problem, the superposition is such that very close to each BH, the metric and extrinsic curvature are exactly Kerr [46], or exactly flat (through attenuation). We then simultaneously solve the Hamiltonian and momentum constraints for an overall conformal factor for the metric and nonsingular correction to the extrinsic curvature using a modification of the TwoPunctures [47] spectral initial data solver. We refer to this extension as Highly Spinning Initial Data (HiSpID, pronounced "high speed").

We evolve these data sets for black-hole binaries from rest and find that the spurious initial radiation is significantly reduced compared to BY initial data (for $\chi \leq 0.9$). Ideally, one would want to use data that had incorporated the exact radiation content of a binary inspiraling from infinity (for post-Newtonian inspired radiation content into the initial data ansatz, see for example [48–51]), but failing this, one at least wants to minimize the nonphysical radiation. Furthermore, it is this spurious radiation (or more precisely, the part of this radiation that is absorbed by the black holes) that prevents conformally flat data from modeling black holes with spins larger than ∼0.93 (see, e.g., Fig. 3 below). Thus by using the HiSpID data, we both get more accurate waveforms for moderate-spin binaries and can go beyond the BY limit to at least $\chi = 0.99$, which has not been possible before for moving puncture codes.

We also consider Lorentz-boosted Schwarzschild BHs in a quasicircular orbital configuration. Here too, it is important to minimize the spurious radiation content of the initial data in order to achieve a very accurate gravitational waveform computation. We again compare with the new data with equivalent BY binaries. BY binaries are also limited in the maximum boost the BHs can have ($P/M_{\rm ADM} = 0.897$, see Ref. [52]), while the HiSpID data can be used to boost BHs in excess of $P/M_{\rm ADM} = 4$ [53].

Finally we address the extremely important problem of modeling highly spinning black holes in quasicircular orbits. For moderate spins ($\chi \lesssim 0.9$), we find that the HiSpID data reproduces the dynamics seen in BY binaries, but again, with substantially lower spurious radiation. BY data cannot model highly spinning binaries. We thus compare our simulation of a $\chi = 0.95$ quasicircular binary with those produced by the SXS Collaboration [17,54,55]. We find excellent agreement between the two methods. The moving puncture approach is used in the open source EinsteinToolkit and by many groups worldwide. The HiSpID approach thus opens up the possibility for numerical evolutions of highly spinning binaries by numerical relativists worldwide.

This paper is organized as follows. In Sec. II we present the formalism to solve for the initial data. We choose the standard transverse-traceless version since it provides the simplest set of equations and allows one to both achieve a reduction of the spurious initial radiation content and overcome the technical limits of the conformally flat initial data reaching highly spinning BHs and highly relativistic velocities. We describe the explicit conformal decomposition and attenuation functions used to regularize the superposition of boosted conformal Kerr/Schwarzschild BHs in the puncture approach.

In Sec. III we describe the numerical techniques to solve for the initial data as an extension of those used to solve the Hamiltonian constraint with the TwoPunctures code. We also provide a summary of the evolution techniques used in the regime of parameters previously unexplored with the moving puncture approach.

In Sec. IV A we show the convergence with spectral collocation points of the spinning initial data to levels of

accuracy acceptable for evolution. We compare waveforms from the new HiSpID initial data to those of the standard spinning BY solution for $\chi = 0.90$. We then evolve highly spinning BHs with $\chi = 0.99$ from rest and discuss the results for the radiated energy and momenta as well as the horizon measures of mass and spin for the individual and final BHs.

In Sec. IV B we show the convergence with spectral collocation points of the initial data for nonspinning Lorentz-boosted BHs. We compare waveforms for our new initial data with the standard boosted BY solution in quasicircular orbit to highlight the benefits of the lower initial spurious radiation of our data.

In Sec. IV C we pursue the study of more generic spinning and orbiting black-hole-binary systems, including binaries with intrinsic spin magnitude $\chi_i = 0.95$. We perform two numerical evolutions at different initial separations and compare them with those performed by the SXS Collaboration finding excellent agreement for both the waveforms and the final remnant.

In the discussion in Sec. V we summarize the results and consider the next series of developments for the initial data and evolution of BHBs.

In the appendixes we study how the initial choice of the lapse and its subsequent gauge evolution [56] affects the accuracy of the simulation at the typical marginal resolutions used to evolve highly spinning BHs, orbiting BHs, and in high-energy head-on BH collisions. We also give the explicit definitions used to compute the Arnowitt-Deser-Misner (ADM) mass and momenta of our initial data.

Throughout this paper we use geometric units where $G = 1$ and $c = 1$. The vacuum Einstein equations are scale invariant in the sense that if we rescale all masses, times, distances, momenta, etc., by the appropriate factor, we obtain an equivalent solution. In the case of a black-hole binary, this amounts to rescaling the total mass while keeping the mass ratio fixed, keeping the dimensionless spins fixed, and rescaling the momenta by the same factor as the masses. When reporting quantities with dimension, we rescale each by an appropriate power of an arbitrary positive constant M (which has dimensions of mass).

II. INITIAL DATA

In this section, we summarize the initial data formalism used to describe BHBs with spin magnitudes up to near maximal. First, we review the conformal decomposition of general relativity's field equations into a set of constraint and evolution equations. Then, we discuss methods for generating the necessary background metric and extrinsic curvature and provide detailed expressions for these in simple cases. Finally, we demonstrate methods for ameliorating effects of singularities at the punctures that allow us to find solutions to the elliptical constraint equations using numerical pseudospectral methods.

A. Constraints

In the Cauchy problem of general relativity, the four-dimensional pseudo-Riemannian spacetime manifold is foliated into three-dimensional spatial hypersurfaces Σ_t, parametrized as surfaces where the time function t is constant. Vacuum solutions to general relativity's field equations on the initial slice $\Sigma_0 = \Sigma_{t=0}$ must satisfy [57]

$$\mathcal{H} \equiv R + K^2 - K_{ij}K^{ij} = 0, \tag{1}$$

$$\mathcal{M}^i \equiv D_j(K^{ij} - \gamma^{ij}K) = 0, \tag{2}$$

known, respectively, as the Hamiltonian and momentum constraints. Latin indices represent spatial degrees of freedom. Here, γ_{ij} is the induced spatial metric tensor on Σ_0 with the associated covariant derivative D_i, and $R = \gamma^{ij}R_{ij}$ is the trace of the spatial Ricci tensor R_{ij}. The extrinsic curvature tensor of Σ_0 and its trace (the mean curvature) are denoted by K_{ij} and $K = \gamma^{ij}K_{ij}$, respectively.

In the conformal transverse-traceless (CTT) formalism [34–36,58], the constraints (1) and (2) become a set of elliptic differential equations for a conformal factor, ψ, and an auxiliary vector, b^i.

The conformal factor relates the physical metric γ_{ij} of the initial slice to a conformally related metric $\tilde{\gamma}_{ij}$ by

$$\gamma_{ij} = \psi^4\tilde{\gamma}_{ij}.$$

All quantities with a tilde are associated with $\tilde{\gamma}_{ij}$. The conformal factor ψ is a scalar function that is everywhere positive. The extrinsic curvature tensor is split into trace and trace-free parts

$$K_{ij} = A_{ij} + \frac{1}{3}\gamma_{ij}K. \tag{3}$$

It is convenient to adopt the conformal rescaling

$$A_{ij} = \psi^{-2}\tilde{A}_{ij}, \tag{4}$$

while leaving the mean curvature conformally invariant, $K = \tilde{K}$. CTT splits $\tilde{A}_{ij}$ into a symmetric, trace-free part and a longitudinal part:

$$\tilde{A}_{ij} = \tilde{M}_{ij} + \frac{1}{\tilde{\sigma}}(\tilde{\mathbb{L}}b)_{ij}, \tag{5}$$

where $\tilde{\sigma}$ is a positive definite scalar and the longitudinal vector derivative acting on b^i is defined by

$$(\tilde{\mathbb{L}}b)_{ij} \equiv \tilde{D}_i b_j + \tilde{D}_j b_i - \frac{2}{3}\tilde{\gamma}_{ij}\tilde{D}_k b^k.$$

In the CTT formalism, the freely specifiable degrees of freedom are contained in $\tilde{\gamma}_{ij}$, $\tilde{M}_{ij}$, K, and $\tilde{\sigma}$. In the case with

no boost, the Kerr metric admits spatial hypersurfaces satisfying the maximal slicing condition $K = 0$ [33]. We will adopt nontrivial K for the boosted case (see Sec. II B 2). For simplicity, we set $\tilde{\sigma} = 1$ everywhere. With these choices, the constraint equations (1) and (2) become

$$\tilde{D}^2\psi - \frac{\psi\tilde{R}}{8} - \frac{\psi^5 K^2}{12} + \frac{\tilde{A}_{ij}\tilde{A}^{ij}}{8\psi^7} = 0, \tag{6}$$

$$\tilde{D}_j\tilde{A}^{ij} - \frac{2}{3}\psi^6\tilde{\gamma}^{ij}\tilde{D}_j K = 0, \tag{7}$$

where $\tilde{D}^2 \equiv \tilde{\gamma}^{ij}\tilde{D}_i\tilde{D}_j$.

B. Background metric

To calculate the spatial metric and extrinsic curvature associated with a boosted black hole of mass m, linear 3-momentum P^i, and spin S^i, we Lorentz boost the four-dimensional Kerr (Schwarzschild in the case were $S = 0$) line element in Cartesian coordinates (we discuss specific coordinate systems below). We then extract from the transformed metric the spatial metric γ^*_{ij}, the lapse function α^*, and the shift vector β^i_* (a super-/subscript $*$ indicates that this is a single black-hole quantity). We then obtain the extrinsic curvature K^*_{ij} on Σ_0 using the evolution equation for the spatial metric

$$K^*_{ij} = \frac{1}{2\alpha^*}(D^*_i\beta^*_j + D^*_j\beta^*_i - \partial_t\gamma^*_{ij}). \tag{8}$$

CTT separates this into trace and trace-free parts

$$K^*_{ij} = \psi_*^{-2}\tilde{A}^*_{ij} + \frac{1}{3}\psi_*^4\tilde{\gamma}^*_{ij}K^*,$$

where $K^* = \gamma^{*ij}_* K^*_{ij}$. When factoring γ_{ij} into $\gamma_{ij} = \psi^4\tilde{\gamma}_{ij}$, any choice of positive function ψ will lead to a valid elliptical constraint system outside the black holes. In the puncture approach [59], one chooses the conformal factor ψ so that the resulting conformally related metric is nonsingular. This can be accomplished in several ways. For example, one can choose to include only the leading-order contributions to the background conformal factor, i.e., $\psi^* = 1 + \frac{\sqrt{m^2-a^2}}{2r}$, where r is the quasi-isotropic radius, or more complete expressions, as detailed in the next section.

Our black-hole-binary initial data is constructed using a superposition of metric and extrinsic curvature terms derived from the above expressions. To distinguish contributions for the two black holes, we replace the $*$ super-/subscript above with a $+$ or $-$.

The trace-free part of the extrinsic curvature is split into background terms $\tilde{M}_{ij}$ and a longitudinal correction term obtained from a vector b_i. Here

$$\tilde{M}_{ij} = \tilde{A}^{(+)}_{ij} + \tilde{A}^{(-)}_{ij}, \tag{9}$$

where $\tilde{A}^{(+)}_{ij}$ and $\tilde{A}^{(-)}_{ij}$ are the trace-free part of the conformal extrinsic curvature of a single boosted Kerr (Schwarzschild) black holes located at $\vec{r} = \vec{r}_+$ and $\vec{r} = \vec{r}_-$. Note that the trace-free part of the single boosted black-hole extrinsic curvature will have a small trace with respect to a metric constructed by superimposing two different background metrics. We remove this extra trace term prior to solving the initial data equations, i.e., $\tilde{M}_{ij} \to \tilde{M}_{ij} - \frac{1}{3}\tilde{\gamma}_{ij}\tilde{\gamma}^{lm}\tilde{M}_{lm}$ (where $\tilde{\gamma}_{ij}$ is the superimposed background metric). The complete trace-free part of the extrinsic curvature for the superimposed spacetime is given by Eq. (5).

In practice, we do not derive analytical expressions for γ_{ij} and K_{ij} for all possible boosts and spin orientations. Rather, we evaluate the unboosted Kerr metric and its first and second derivatives pointwise, and then apply a boost and rotations to the metric (and the corresponding transformation of the derivatives of the metric) and then algebraically solve for γ_{ij} and K_{ij} at that point. In the subsections below, we provide explicit formulas for these quantities for the cases of nonboosted Kerr and boosted Schwarzschild spacetimes.

1. Conformal Kerr

In spherical quasi-isotropic coordinates, the Kerr conformal spatial line element is [33,60]

$$\mathrm{d}\tilde{\ell}^2 = \tilde{\gamma}_{ij}\mathrm{d}x^i\mathrm{d}x^j = \mathrm{d}r^2 + r^2\mathrm{d}\Omega^2 + a^2hr^4\sin^4(\theta)\mathrm{d}\varphi^2,$$

where m is the puncture mass, a is the angular momentum per unit mass, r is the quasi-isotropic radial coordinate, $\mathrm{d}\Omega$ is the unit sphere line element, and [40]

$$\bar{r} = r + m + \frac{m^2 - a^2}{4r},$$
$$\Sigma = \bar{r}^2 + a^2\cos^2(\theta),$$
$$\sigma = \frac{2m\bar{r}}{\Sigma},$$
$$h = \frac{1+\sigma}{\Sigma r^2}.$$

The nonvanishing component of the shift vector is

$$\beta^\varphi = -\frac{2amr}{(r^2+a^2)^2 - a^2(r^2 - 2mr + a^2)\sin^2(\theta)}.$$

The nonvanishing components of the conformal extrinsic curvature associated with this metric are given by [33,60,61]

$$\tilde{A}_{r\varphi} = \frac{H_E\sin^2(\theta)}{r^2},$$
$$\tilde{A}_{\theta\varphi} = \frac{H_F\sin(\theta)}{r},$$

with the definitions

$$e^{-2q} = \frac{\Sigma}{\bar{r}^2 + a^2[1+\sigma\sin^2(\theta)]},$$
$$H_E = e^{-q}\frac{am}{\Sigma^2}[(\bar{r}^2 - a^2)\Sigma + 2\bar{r}^2(\bar{r}^2 + a^2)],$$
$$H_F = e^{-q}\frac{a^3 m\bar{r}}{2r\Sigma^2}(m^2 - a^2 - 4r^2)\cos(\theta)\sin^2(\theta).$$

The Kerr metric in quasi-isotropic coordinates admits spatial hypersurfaces satisfying the maximal slicing condition $K = 0$ [33].

The quasi-isotropic Kerr conformal factor is

$$\psi_{\rm QI} = \left(\frac{\Sigma}{r^2}\right)^{1/4}. \tag{10}$$

Ultimately, only the asymptotic behavior is important, so sometimes just the lowest order terms of $\psi_{\rm QI}$ are used [40]:

$$\psi_{\rm QI} \approx 1 + \frac{\sqrt{m^2 - a^2}}{2r}.$$

Near the puncture

$$\tilde{R} = -\frac{96a^2}{(m^2 - a^2)^2} + \mathcal{O}(r^2)$$

and

$$\tilde{D}^2\psi_{\rm QI} = -\frac{6a^2}{(m^2 - a^2)^{3/2}r} - \frac{12ma^2}{(m^2 - a^2)^{5/2}} + \mathcal{O}(r).$$

It follows that

$$\tilde{D}^2\psi_{\rm QI} - \frac{1}{8}\psi_{\rm QI}\tilde{R} = -\frac{288m^2a^2r\sin^2(\theta)}{(m^2 - a^2)^{7/2}} + \mathcal{O}(r^2). \tag{11}$$

All fields are transformed to a Cartesian basis, with coordinates related by

$$x = r\sin(\theta)\cos(\varphi),$$
$$y = r\sin(\theta)\sin(\varphi),$$
$$z = r\cos(\theta). \tag{12}$$

The conformal spatial metric takes the form

$$\tilde{\gamma}_{ij} = \delta_{ij} + a^2 h v_{ij},$$

where δ_{ij} is the Kronecker delta and

$$v_{ij} = \begin{pmatrix} y^2 & -xy & 0 \\ -xy & x^2 & 0 \\ 0 & 0 & 0 \end{pmatrix}.$$

The nonvanishing Cartesian components of the trace-free conformal extrinsic curvature tensor are

$$\tilde{A}_{xx} = -\tilde{A}_{yy} = -\frac{2H_1\sin(\varphi)\cos(\varphi)}{r^3},$$
$$\tilde{A}_{xy} = \frac{H_1\cos(2\theta)}{r^3},$$
$$\tilde{A}_{xz} = \frac{H_2\sin(\theta)\sin(\varphi)}{r^3},$$
$$\tilde{A}_{yz} = -\frac{H_2\sin(\theta)\cos(\varphi)}{r^3},$$

where

$$H_1 = H_F\cos(\theta) + H_E\sin^2(\theta),$$
$$H_2 = H_F - H_E\cos(\theta).$$

At the puncture, these functions have the series expansion

$$H_1 \sim 3am\sin^2(\theta) + \mathcal{O}(r^2),$$
$$H_2 \sim -3am\cos(\theta) + \mathcal{O}(r^2).$$

Thus, in Cartesian coordinates $\tilde{A}_{ij} \sim \mathcal{O}(1/r^3)$ at the puncture. At this point, the spin is parallel to the z axis. In our approach, we specify the direction and magnitude of the angular momentum $\vec{S}$ of each black hole. For a given black hole, this means that we choose the Kerr parameter a such that $a = |\vec{S}|/m$, and rotate all fields so that the spin points along $\vec{S}$.

2. Conformal Lorentz-boosted Schwarzschild

To describe a nonspinning BH with an arbitrary linear momentum P^i, we begin with the Schwarzschild line element in isotropic Cartesian coordinates (t_0, x_0, y_0, z_0):

$$ds^2 = -\alpha_0^2 dt_0^2 + \psi_0^4(dx_0^2 + dy_0^2 + dz_0^2),$$

where

$$\alpha_0 = \frac{1 - \frac{m}{2r_0}}{1 + \frac{m}{2r_0}}$$

is the lapse,

$$\psi_0 = 1 + \frac{m}{2r_0}$$

is the puncture conformal factor, and $r_0 = \sqrt{x_0^2 + y_0^2 + z_0^2}$. Next, we perform a Lorentz transformation in the y_0 direction, with the associated change of variables

$$\begin{aligned} t_0 &= \gamma(t - vy), \\ x_0 &= x, \\ y_0 &= \gamma(y - vt), \\ z_0 &= z, \end{aligned}$$

where (t, x, y, z) are the coordinates of the boosted reference frame, v is the magnitude of the local velocity vector

$$v^i = \frac{P^i}{\sqrt{m^2 + P^j P_j}},$$

and $\gamma = (1 - v^2)^{-1/2}$. Afterward, all of the fields are rotated such that they are oriented in the desired direction, momentum aligned with P^i.

From the boosted spacetime metric, we extract the lapse function, shift vector, and spatial metric. The only nonvanishing component of the shift is

$$\beta^y = -\frac{mv(m^2+6mr+16r^2)(m^3+6m^2r+8mr^2+16r^3)}{B^2},$$

with

$$B = \sqrt{(m+2r)^6 - 16(m-2r)^2 r^4 v^2}.$$

On the $t_0 = 0$ hypersurface, $r_0 \to r = \sqrt{x^2 + y^2\gamma^2 + z^2}$ and the conformal factor is

$$\psi_{\rm B} = 1 + \frac{m}{2r}.$$

The conformal spatial line element on Σ_0 is

$$d\tilde{\ell}^2 = dx^2 + \gamma^2\left[1 - \frac{16(m-2r)^2 r^4 v^2}{(m+2r)^6}\right]dy^2 + dz^2.$$

Near the puncture

$$\tilde{R} = \frac{32v^2[7 + \cos(2\theta) + 2\sin^2(\theta)\cos(2\varphi)]r^2}{m^4} + \mathcal{O}(r^3) \tag{13}$$

and

$$\tilde{D}^2\psi_{\rm B} = \frac{8v^2[\cos^2(\theta) + \sin^2(\theta)\cos^2(\varphi)]r}{m^3} + \mathcal{O}(r^2), \tag{14}$$

with coordinates θ and φ defined by (12).

The evolution equation for the spatial metric gives us an expression for the extrinsic curvature

$$K_{ij} = \frac{1}{2\alpha}(D_i\beta_j + D_j\beta_i - \partial_t\gamma_{ij}).$$

The mean curvature is

$$K = \frac{32\gamma mv[(m+2r)^7 - 32(m-2r)^2(m-r)r^4v^2]r^2 y}{(m+2r)^3 B^3}.$$

The nonvanishing components of the trace-free, conformal extrinsic curvature tensor are

$$\begin{aligned} \tilde{A}_{xx} &= \tilde{A}_{zz} = \frac{\gamma mv(m-4r)(m+2r)^3 BCy}{3Dr^4}, \\ \tilde{A}_{xy} &= -\frac{\gamma mv(m-4r)(m+2r)^3 x}{2Br^4}, \\ \tilde{A}_{yy} &= -\frac{2\gamma^3 mv(m-4r)Cy}{3(m+2r)^3 Br^4}, \\ \tilde{A}_{yz} &= -\frac{\gamma mv(m-4r)(m+2r)^3 z}{2Br^4}, \end{aligned}$$

with

$$\begin{aligned} C &= (m+2r)^6 - 8(m-2r)^2 r^4 v^2, \\ D &= (m+2r)^{12} - 32(m-2r)^2 r^4 (m+2r)^6 v^2 \\ &\quad + 256(m-2r)^4 r^8 v^4. \end{aligned}$$

We see in Cartesian coordinates that $\tilde{A}_{ij} \sim \mathcal{O}(1/r^2)$ and $K \sim \mathcal{O}(r^3)$ at the puncture.

3. Kerr with arbitrary spin orientations and boosts

In this section we describe how we construct the background metric ($\tilde{\gamma}_{ij}$) and extrinsic curvature (K and $\tilde{M}_{ij}$) for binaries with generic spin orientations and arbitrary momenta. Due to the complexity of the expressions, we do not calculate the extrinsic curvature in closed form. Rather, we start by calculating the Kerr 4-metric in various gauges and then perform rotations and boosts. Specifically, we start with the Kerr metric in quasi-isotropic coordinates. In the text below we will refer to quasi-isotropic coordinates as QI coordinates. QI coordinates have the unfortunate property that the horizon coordinate size goes to zero as the spin becomes maximal. We ameliorate this problem by introducing a radial *fish-eye* [62] transformation that increases the horizon's radius. A fish-eye transformation has the general form

$$R = rf(r), \tag{15}$$

where R is the new radial coordinate, r is the original radial coordinate, and if $f(r)$ can be expanded as an even power

series in r, then the transformation is guaranteed to be C^∞ (this is sufficient, but not necessary). These types of coordinates have a long history of use for implementing fixed-mesh refinement within unigrid codes (see, e.g., [4,62–64]). When studying evolutions of single black holes, Liu, Etienne, and Shapiro [65] found a fish-eye–like coordinate system, which we will refer to as LES coordinates here, that has a finite horizon coordinate radius for all values of the spin (the metric is, however, singular for maximal spin). The LES radius can be obtained from the implicit relationship

$$R_{\rm LES}\left(1+\frac{r_+}{4R_{\rm LES}}\right)^2 = r_{\rm QI}\left(1+\frac{m+a}{2r_{\rm QI}}\right)\left(1+\frac{m-a}{2r_{\rm QI}}\right), \tag{16}$$

where $R_{\rm LES}$ is the LES radius, $r_{\rm QI}$ is the quasi-isotropic radius, and $r_+ = m+\sqrt{m^2-a^2}$.

In addition to the quasi-isotropic and LES coordinates, we also consider another radial transformation of the quasi-isotropic radius that allows us to fine-tune the horizon radius. These coordinates, which we will refer to as fish-eye (FE) coordinates are obtained from $R_{\rm FE} = r_{\rm QI}[1-A\exp(-r_{\rm QI}^2/s^2)]$, where A and s are parameters. These coordinates have the property that at large $r_{\rm QI}$, $R_{\rm FE}\approx r_{\rm QI}$, and at small $r_{\rm QI}$, $dR_{\rm FE} = (1-A)dr_{\rm QI}$. Finally, for brevity, we will refer to the standard quasi-isotropic coordinates as QI coordinates here.

Our procedure is as follows. We start with the Kerr metric in QI, LES, or FE coordinates and then transform to Cartesian coordinates defined by $x = r\sin\theta\cos\phi$, etc., where $(r,\ \theta,\ \phi)$ are the QI, LES, or FE coordinates. If the desired spin direction is not aligned with the z, we perform a rotation about the center of the BH to align the spin with the desired direction. We then perform a boost on the resulting metric. In addition to the metric, we also calculate its first and second derivatives by applying the above rotation and boost to the known derivatives of the Kerr metric in the QI, LES, or FE coordinates.

Given the 4-metric and its derivatives in the desired rotated and boosted coordinates at a given point, we calculate the 3-metric and extrinsic curvature via Eq. (8). There is a complication here because in all cases, the lapse goes to zero on the horizon. This leads to severe round-off issues in double precision calculation. To ameliorate this, we calculate the metric and its derivatives to high precision using the MPFR C++ [66] wrapper for the MPFR [67] high-precision library. Due to the expense of using these libraries, we only use them in a small volume around the horizon where high precision is needed.

Next we extract a conformal factor ψ^* so that $\tilde{\gamma}^*_{ij}$ has unit determinant. We then calculate the first and second derivatives of ψ^* and the metric $\tilde{\gamma}^*_{ij}$, as well as the first derivative of the trace-free part of the conformal extrinsic curvature $\tilde{A}^*_{ij}$ and the trace K.

We then perform a series of optional modifications to the metric. First, we can attenuate the metric to a flat metric far from the BH. For this, we use a simple attenuation function

$$\tilde{\gamma}_{ij}-\delta_{ij} \to F(r)(\tilde{\gamma}_{ij}-\delta_{ij}), \tag{17}$$

$$\psi^*-1 \to F(r)(\psi^*-1), \tag{18}$$

$$K^* \to F(r)K^*, \tag{19}$$

$$F(r) = e^{-(r/s)^4}, \tag{20}$$

where r is the coordinate distance to the BH and the parameter s is of order 20–100 (note that we do not attenuate $\tilde{A}_{ij}$). When applying this attenuation, we ensure that all derivatives are modified such that they are consistent with the attenuated functions.

This attenuation ensures that the metric is flat at infinity. If it is not applied, the coordinate components of the resulting metric will have an angular dependent monopole term, i.e., the falloff of the diagonal components will be of the form $1+f(\theta,\phi)/r+\cdots$, where $f(\theta,\phi)$ is a nontrivial function rather than $M_{\rm ADM}/2$. As we would expect that the leading-order effects of an extended body on distant geodesics to be spherically symmetric, this choice of initial data leads to a coordinate system that obscures this symmetry. More importantly, the angular dependence of the background metric at infinity will induce logarithmic terms in the correction functions, which will reduce the order of convergence of the solver.

One drawback of this construction is that by avoiding the derivation of explicit analytical forms for the metric and extrinsic curvature, a process for removing the singularities in a manner consistent with the constraint equations is not apparent. In this paper, we address this issue by modifying the elliptical constraint equations inside the puncture, as described in the next section.

C. Punctures

We use an extended version TwoPunctures [47] thorn to generate puncture initial data for black-hole-binary simulations.

If the constraint equations with a zero right-hand side [Eqs. (1) and (2)] are solved everywhere, then the resulting spacetime would have zero ADM mass, linear, and angular momentum. In the puncture approach, this is circumvented by finding singular solutions to the constraint equations where the source terms are δ functions centered on the two black holes.

In the puncture approach to the CTT formalism [34–36,58], we decompose the conformal factor into singular parts plus a finite correction, u,

$$\psi = \psi_{(+)} + \psi_{(-)} - 1 + u, \tag{21}$$

where $\psi_{(\pm)}$ represents the conformal factors associated with the individual, isolated black holes located at positions labeled as $(+)$ and $(-)$, with the spatial metric tensors $\tilde{\gamma}^{(\pm)}_{ij}$.

Similarly, we decompose $\tilde{A}_{ij}$ into a sum of singular terms (here denoted by $\tilde{M}_{ij}$) and a nonsingular correction $(\tilde{\mathbb{L}}b)_{ij}$.

In addition to the required singular longitudinal component of $\tilde{M}_{ij}$, there are nonsingular longitudinal components as well. These extra nonsingular components are removed by the inclusion of $(\tilde{\mathbb{L}}b)_{ij}$ (see, e.g., [58,68]).

In order to deal with the puncture singularities, we introduce modifications (in the form of attenuation functions) to both the background metric and the mean curvature, as well as modifications to the singular source terms inside the horizons themselves. The first type of modification is consistent with the Einstein constraint equations everywhere and has the form,

$$\tilde{\gamma}_{ij} = \delta_{ij} + f_{(+)}(\tilde{\gamma}^{(+)}_{ij} - \delta_{ij}) + f_{(-)}(\tilde{\gamma}^{(-)}_{ij} - \delta_{ij}), \tag{22}$$

$$\tilde{M}_{ij} = \tilde{A}^{(+)}_{ij} + \tilde{A}^{(-)}_{ij}, \tag{23}$$

$$K = f_{(+)}K_{(+)} + f_{(-)}K_{(-)}, \tag{24}$$

$$\Psi = \psi_{(+)} + \psi_{(-)} - 1, \tag{25}$$

where

$$f_{(\pm)} = 1 - e^{-(r_{(\mp)}/\omega_{(\pm)})^p},$$

and $r_{(\pm)}$ is the coordinate distance from a field point to the location of puncture $(\pm)$. The parameters $\omega_{(\pm)}$ control the steepness of the attenuation and p controls how many derivatives of the attenuated function are zero at the origin. We explain how this can be effective at removing certain singularities, and its limitations, below.

This type of attenuation, by itself, is sufficient for superimposed boosted Schwarzschild BHs or superimposed unboosted Kerr BHs. However, for the more general case we found that modifying the equations themselves inside the BHs was needed for satisfactory convergence of the constraints outside the horizons. This modification, which also comes in the form of a smooth attenuation function, has the effect of introducing constraint violations inside the horizons. The constraint violations induced by these modifications are not necessarily small, nor does the resulting *fictitious matter* have to obey any of the standard energy conditions. Fortunately, as shown in [69,70], constraint violating modes for standard Baumgarte-Shapiro-Shibata-Nakamura (BSSN) and Z4 systems are causal, i.e., they must stay inside the horizons. Hence the resulting numerical spacetime will be a valid solution of the vacuum Einstein equations outside the horizons.

The modified Hamiltonian and momentum constraint equations for the correction functions u and b^i are

$$\tilde{D}^2 u - g\frac{\psi\tilde{R}}{8} - g\frac{\psi^5 K^2}{12} + g\frac{\tilde{A}_{ij}\tilde{A}^{ij}}{8\psi^7} + g\tilde{D}^2(\psi_{(+)} + \psi_{(-)}) = 0, \tag{26a}$$

$$\tilde{\Delta}_{\mathbb{L}} b^i + g\tilde{D}_j\tilde{M}^{ij} - g\frac{2}{3}\psi^6\tilde{\gamma}^{ij}\tilde{D}_j K = 0, \tag{26b}$$

where $\tilde{\Delta}_{\mathbb{L}} b^i \equiv \tilde{D}_j(\tilde{\mathbb{L}}b)^{ij}$ is the vector Laplacian and $\tilde{R}$ is the scalar curvature associated with $\tilde{\gamma}_{ij}$, and where the attenuation function g takes the form

$$g = g_+ \times g_-,$$

$$g_\pm = \begin{cases} 1 & \text{if } r_\pm > r_{\max} \\ 0 & \text{if } r_\pm < r_{\min} \\ \mathcal{G}(r_\pm) & \text{otherwise,} \end{cases}$$

$$\mathcal{G}(r_\pm) = \frac{1}{2}\left[1 + \tanh\left(\tan\left[\frac{\pi}{2}\left(-1 + 2\frac{r_\pm - r_{\min}}{r_{\max} - r_{\min}}\right)\right]\right)\right],$$

and the parameters $r_{\min} < r_{\max}$ are chosen to be within the horizon. In addition, we can optionally attenuate the background metric itself when calculating the $\tilde{D}^2 u$ and $\tilde{\Delta}_{\mathbb{L}} b^i$. To do this we take

$$\tilde{\gamma}_{ij} \to \delta_{ij} + g(r)(\tilde{\gamma}_{ij} - \delta_{ij}), \tag{27}$$

$$\tilde{\Gamma}^k_{ij} \to g(r)\tilde{\Gamma}^k_{ij}. \tag{28}$$

Note that the modified $\tilde{\Gamma}^k_{ij}$ is not consistent with the modified $\tilde{\gamma}_{ij}$. There is no advantage to making them consistent because the constraints will be violated in the attenuation zone regardless. By modifying the metric in this way, we can ensure that the elliptical system has exactly the form of the flat space Poisson system in the vicinity of the punctures.

To understand the limitations of using the f attenuation alone, consider Eqs. (26a) and (26b) at the location of puncture $+$ assuming the background contributions of puncture $-$ are attenuated to zero in the vicinity of puncture $+$. Since the background fields $\tilde{\gamma}_{ij} = \tilde{\gamma}^+_{ij}$, $\psi = \psi_+$, $K = K_+$, $\tilde{M}_{ij} = \tilde{M}^+_{ij}$ obey the constraints exactly, these equations reduce to (note $\psi_- = 0$, $M^-_{ij} = 0$)

$$\tilde{D}^2 u - \frac{u\tilde{R}}{8} - \frac{\psi_+^5 K^2}{12}\left(\left(1+\frac{u}{\psi_+}\right)^5 - 1\right) + \frac{\tilde{M}_{ij}\tilde{M}^{ij}}{8\psi_+^7}\left(\left(\frac{1}{1+u/\psi_+}\right)^7 - 1\right) + \frac{\tilde{A}_{ij}\tilde{A}^{ij} - \tilde{M}_{ij}\tilde{M}^{ij}}{8\psi_+^7}\left(\left(\frac{1}{1+u/\psi_+}\right)^7\right) = 0,$$

$$\tilde{\Delta}_{\mathbb{L}} b^i - \frac{2}{3}\psi_+^6((1+u/\psi_+)^6 - 1)\tilde{\gamma}^{ij}\tilde{D}_j K = 0.$$

Since ψ_+ is singular at puncture $+$, these equations are nonsingular on the puncture only if $\tilde{R}$ is finite and K goes to zero sufficiently rapidly. The latter condition, in particular, cannot always be guaranteed. In addition, the operators $\tilde{D}^2$ and $\tilde{\Delta}_{\mathbb{L}}$ themselves need to be nonsingular on the puncture. Hence the use of the g attenuation which explicitly modifies these terms to guarantee smooth behavior.

In addition, the form of the superimposed boosted Kerr background itself induces logarithmic terms in the $1/r$ expansion of u [71]. While u may still be formally finite, these logarithmic terms reduce the order of convergence of spectral expansions. This can be overcome by attenuating the metric at large distances so that it is conformally flat. Note that modifying the background spacetime far away only guarantees that the lowest order (in $1/r$) singular terms are removed. Higher-order terms can still be present, in general.

III. NUMERICAL TECHNIQUES

A. Initial data solver with spectral methods

The standard version of the TwoPunctures thorn [47] generates conformally flat ($\tilde{\gamma}_{ij} = \delta_{ij}$) initial data via a spectral expansion of the Hamiltonian constraint on a compactified collocation point grid. Here we extend this to include both a nonflat background metric and a vector Poisson equation for the b^i in Eq. (26).

This is achieved by extending TwoPunctures to solve for u and b^i simultaneously at each collocation point. The solver handles the nonlinearities in the constraint equations by using a linearized Newton-Raphson method.

The solutions are required to obey the falloff conditions

$$\lim_{r\to\infty} u = 0 \quad \text{and} \quad \lim_{r\to\infty} b^i = 0,$$

which are the only physical boundary conditions for the problem. These are enforced numerically by noting that the TwoPunctures compactified coordinate A obeys $A \to 1$ as $r \to \infty$, thus allowing the asymptotic behavior to be factored out (e.g., write $u = (A-1)U$ and solve for the auxiliary function U) [47].

In our implementation, we enforce a falloff of at least $1/r$ for all fields by requiring that they be zero at infinity. However, we find that the b^i fields fall off faster, as expected given the form of the equations, as shown in Fig. 1.

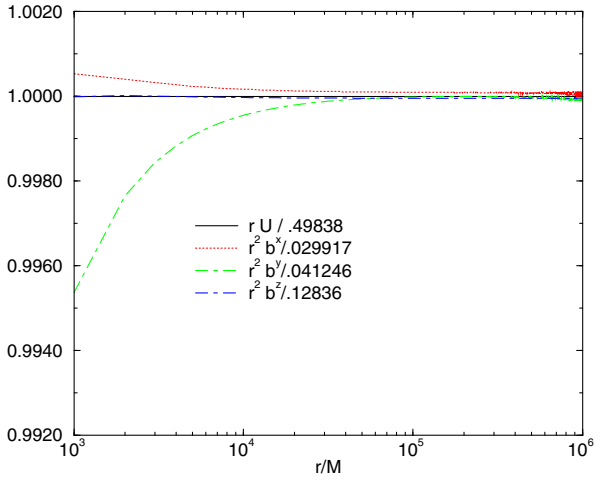

FIG. 1. The falloff with radius of the correction fields u and b^i for a $\chi = 0.95$ binary along the line $x = y = z$. As can be seen, u falls off as $1/r$ and all components of b^i fall off as $1/r^2$. Note that the boundary conditions for b^i only require that the components go to zero at infinity. The quadratic falloff is a consequence of the initial data not having net linear momentum. In addition to multiplying each function by the appropriate power of r, we rescale the resulting curves so that all approach ~ 1 at large r.

As mentioned above, there are several sources of singular behaviors. Briefly, the differential equations themselves can become singular at the punctures, and the behavior of the equations at infinity can induce logarithmic terms in the solution. Regardless, finite-precision effects makes evaluating the Laplacian operator and source terms inaccurate close to the puncture. We overcome both these issues in the general case by enforcing that the background metric is identically flat (with $K = 0$) at large r and sufficiently close to the puncture. Furthermore, close to the puncture, we smoothly attenuate all source terms to zero. Thus in a finite ball surrounding each puncture, the elliptic equations reduce to a source-free Laplacian and a vector Laplacian, respectively. The end result is a well behaved solution to the Einstein constraint system outside the two horizons.

Note that solutions to Eqs. (26a) and (26b) can contain logarithmic terms of the form $r^{-k}\ln r$, where the integer k is determined by the falloff rate of the source terms in the two equations [72]. If such terms are present in the solution, the convergence rate of the solver will be algebraic rather than exponential. In practice, we find that the accuracy of the solver is limited by small-scale features induced by the attenuation functions inside the horizons.

In Eq. (26), derivatives of the background fields $\tilde{\gamma}_{ij}$, $\tilde{M}_{ij}$, and $\psi_\pm$ can be calculated analytically or numerically. We have implemented both approaches. In practice, we use an eighth-order finite difference operator with a step size of $\leq 10^{-4}$ (always smaller than the finest grid spacing) for the QI boosted Kerr (fixed spin direction) and boosted

Schwarzschild data, and analytical expressions for the LES and FE boosted Kerr data derivatives (these latter two are evaluated using the high-precision libraries mentioned above). Note that the accuracy of these derivatives near the punctures is irrelevant inside the attenuation region as these terms get multiplied by zero.

B. Evolution and gauges

We use the extended TwoPunctures thorn to generate puncture initial data [59] for the BHB simulations. These data are characterized by mass parameters m_p (which are not the horizon masses), as well as the momentum and spin of each BH, and their initial coordinate separation. We evolve these BHB data sets using the LazEv [63] implementation of the moving puncture approach with the conformal function $W = \exp(-2\phi)$ suggested by Ref. [73]. For the runs presented here, we use centered, eighth-order finite differencing in space [26] and a fourth-order Runge-Kutta time integrator. (Note that we do not upwind the advection terms.) Our code uses the CACTUS/EinsteinToolkit [42,43] infrastructure. We use the CARPET mesh refinement driver to provide a "moving boxes" style of mesh refinement.

We locate the apparent horizons using the AHFinderDirect code [74] and measure the horizon spin using the isolated horizon algorithm detailed in [75].

For the computation of the radiated angular momentum components, we use formulas based on "flux linkages" [76] and explicitly written in terms of Ψ_4 in [77,78].

We obtain accurate, convergent waveforms and horizon parameters by evolving this system in conjunction with a modified $1+\log$ lapse and a modified Γ-driver shift condition [4,79,80]. The lapse and shift are evolved with

$$(\partial_t - \beta^i \partial_i)\alpha = -\alpha^2 f(\alpha) K, \tag{29a}$$

$$\partial_t \beta^a = \frac{3}{4}\tilde{\Gamma}^a - \eta\beta^a. \tag{29b}$$

In the original moving puncture approach we used $f(\alpha) = 2/\alpha$ and an initial lapse $\alpha(t=0) = \psi_{\rm BL}^{-2}$ [4] or $\alpha(t=0) = 2/(1+\psi_{\rm BL}^4)$ [11], where $\psi_{\rm BL} = 1 + m_{(+)}/(2r_{(+)}) + m_{(-)}/(2r_{(-)})$. In Sec. IV B and Appendix A we also use $\alpha(t=0) = 1/(2\psi_{\rm BL} - 1)$, which seems better suited for the highly spinning or highly boosted BH evolutions. There, we explore other gauge conditions for the lapse in the form of $f(\alpha) = 1/\alpha$ (gauge speed = 1) and $f(\alpha) = 8/(3\alpha(3-\alpha))$ (shock avoiding) [56] which prove to be more convenient when dealing with highly boosted moving punctures.

IV. EVOLUTIONS OF THE HiSpID DATA

In this section we describe results from evolutions of the new HiSpID data for black-hole binaries with spins,

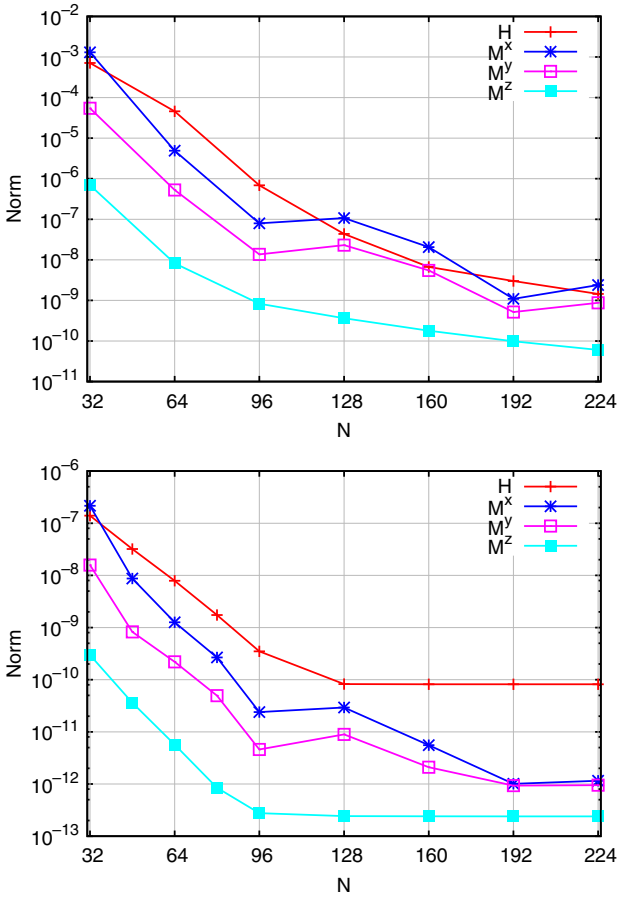

FIG. 2. Convergence of the residuals of the Hamiltonian and momentum constraints versus the number of collocation points N for BHBs with $\chi = 0.99$ in the UU configuration with exponential attenuation parameters $\omega_{(\pm)} = 1.0$ and $p = 4$. (Top panel) For a small grid along the x axis ($4.25 \le x \le 4.75$, $-0.25 \le y \le 0.25$, and $-0.25 \le z \le 0.25$). (Bottom panel) For the full numerical evolution grid.

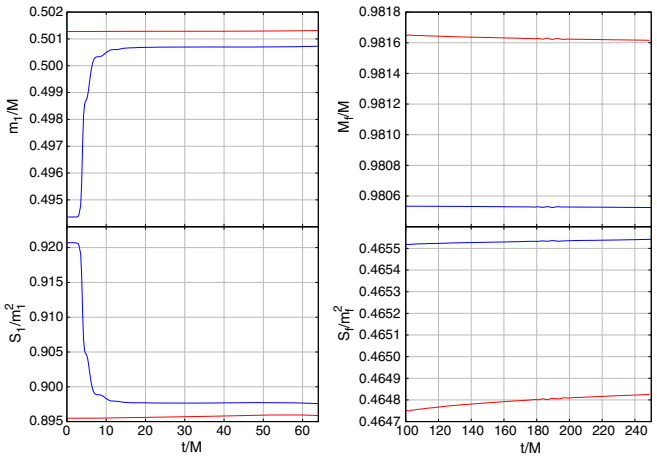

FIG. 3. Masses of the individual BHs from the start of the simulation until merger (top left). Spins of the individual BHs until merger (bottom left). Masses of the remnant BH (top right). Spin of the remnant BH (bottom right). BY, blue; HiSpID, red.

TABLE I. Initial data parameters for the equal-mass, head-on configurations. The punctures are initially at rest and are located at $(\pm b, 0, 0)$ with spins S aligned or antialigned with the z direction, mass parameters $m_{\rm p}$, horizon (Christodoulou) masses $m_1 = m_2 = m_{\rm H}$, total ADM mass $M_{\rm ADM}$, and dimensionless spins $a/m_{\rm H} = S/m_{\rm H}^2$, where $a_1 = a_2 = a$. The Bowen-York configurations are denoted by BY, and the HiSpID by HS. Finally, UU or UD denote the direction of the two spins, both either aligned (UU) or antialigned (UD).

Configuration	b/M	$m_{\rm p}$	S/M^2	$a/m_{\rm H}$	$m_{\rm H}$	$M_{\rm ADM}/M$
BY90UU	6	0.191475	0.225	0.8977	0.500702	0.982362
HS90UU	6	0.5	0.225	0.8958	0.501287	0.982353
BY90UD	6	0.191475	0.225	0.8977	0.500702	0.982396
HS90UD	6	0.5	0.225	0.8955	0.501208	0.982388
HS99UU	6	0.5	0.2475	0.9896	0.500162	0.980124
HS99UD	6	0.5	0.2475	0.9887	0.499981	0.980163

boosts, or both. We start by examining the case of two superimposed Kerr black holes initially at rest. We then examine superimposed boosted Schwarzschild black holes in quasicircular binaries. Next, we compare evolutions of spinning quasicircular binaries with moderate spins using both HiSpID and BY data. Finally, we compare evolutions of a spinning, quasicircular black-hole binary with specific spin $\chi = 0.95$ to results found by the SXS Collaboration [17,54,55] for similar systems.

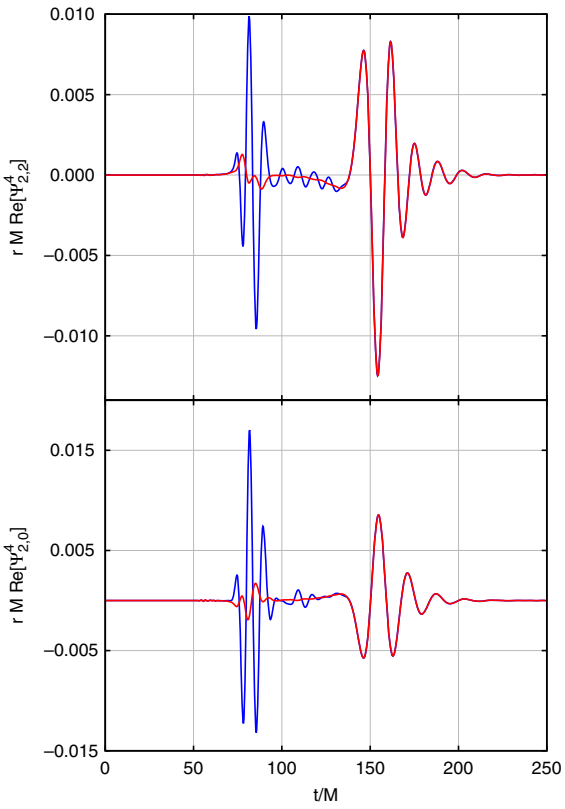

FIG. 4. $(\ell = 2, m = 2)$ mode of Ψ_4 at $r = 75M$ (top panel). (2,0) mode of Ψ_4 at $r = 75M$ (bottom panel) for spinning binaries with $\chi = 0.9$. BY data, blue (showing a much larger initial burst); HiSpID, red.

A. Headon collisions of spinning black holes

We begin our analysis with the case of two spinning black holes initially at rest. This type of system was first analyzed in [40] using a very similar construction (i.e., superimposed Kerr black holes in a puncture gauge).

We begin by demonstrating the convergence of the initial data. As shown in Fig. 2, even at very high spins (here $\chi = 0.99$) the constraints converge to round-off levels. In order to reach acceptable levels of constraint satisfaction, we had to use relatively large numbers of collocation points. Here we used up to 224 collocation points in the two directions orthogonal to the symmetry axis. Because a simple L^2 norm of the constraints may *hide* issues near the black holes, we construct L^2 norms in both a small box near each black hole, and in the bulk of the simulation domain (out to a distance of $30M$ from the origin). Close to the black holes, the constraints continue to reduce with the number of collocation points, falling down to $\mathcal{O}(10^{-9})$. In the bulk, the much smaller L^2 norms fall to round-off levels $\mathcal{O}(10^{-10}) - \mathcal{O}(10^{-12})$ and then remain constant.

As done in [40], we compare the new data to Bowen-York (conformally flat) initial data with the same spin parameters. For given binary separations and spin parameters, the horizon masses and spins for the HiSpID and BY data are not identical, as shown in Fig. 3, since the initial radiation content and distortions are not the same. However, they are close enough for comparisons of physical quantities such as the gravitational waveforms.

TABLE II. The final mass, final remnant spin, and recoil velocity for each configuration.

Configuration	$M_{\rm rem}/M$	$\chi_{\rm rem}$	V
BY90UU	0.98053	0.46554	0
HS90UU	0.98162	0.46483	0
BY90UD	0.98073	0	35.90
HS90UD	0.98181	0	36.01
HS99UU	0.97971	0.52501	0
HS99UD	0.97900	0	38.40

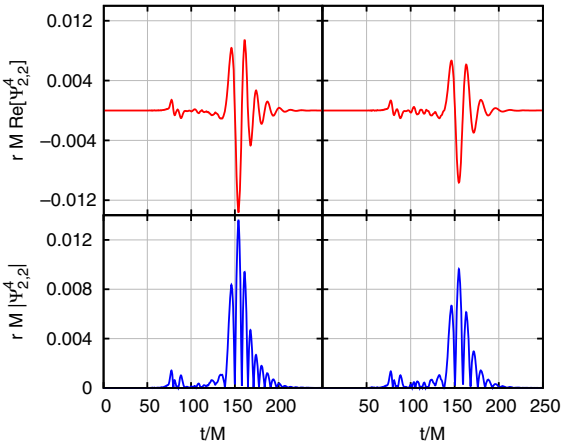

FIG. 5. Waveforms and waveform magnitudes of the UU (left panels) and UD (right panels) configurations with highly spinning BHs $\chi = 0.99$. Note the small amplitude of the initial data radiation content at around $t = 75M$, compared to the merger signal after $t = 130M$.

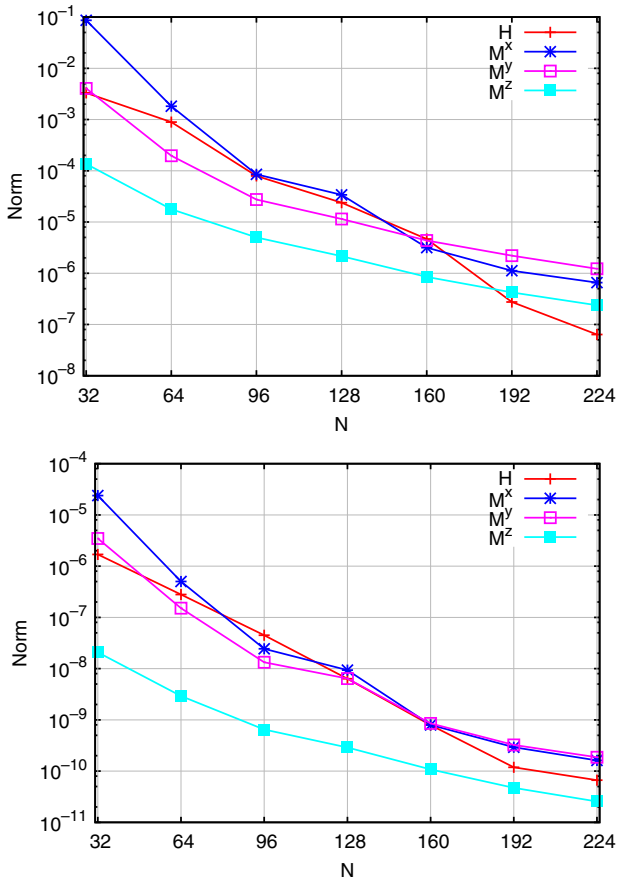

FIG. 6. Convergence of the residuals of the Hamiltonian and momentum constraints versus the number of collocation points N for Schwarzschild BHBs in a quasicircular orbit with exponential attenuation parameters $\omega_{(\pm)} = 1.0$ and $p = 6$. Orbital parameters $P^y = 0.0848M$, $d = 12M$. (Top panel) For a small grid along the x axis ($4.75 \leq x \leq 5.25$, $0.1 \leq y \leq 0.6$, and $0.5 \leq z \leq 1.0$). (Bottom panel) For the full numerical evolution grid.

TABLE III. Initial data parameters for the equal-mass, boosted configurations. The punctures are initially at rest and are located at $(\pm b, 0, 0)$ with momentum $\vec{P} = P_x\hat{x} + P_y\hat{y}$, mass parameters m_p, horizon (Christodoulou) masses m_H, and the total ADM mass M_{ADM}. The configurations are Bowen-York (BY) or Lorentz-boosted (HS) initial data.

Configuration	b/M	m_p	P_x	P_y	m_H	M_{ADM}/M
BYQC	4.7666	0.48523	−0.001153	0.09932	0.5	0.98931
HSQC	4.7666	0.48745	−0.001138	0.09794	0.5	0.98914

TABLE IV. The final mass and spin for each configuration.

Configuration	M_{rem}/M	χ_{rem}
BYQC	0.95162	0.68643
LBQC	0.95155	0.68646

We study a few test cases of equal-mass BHB configurations starting from rest with spins aligned (UU) or counteraligned (UD) with each other, and perpendicular to the line joining the BHs. We evolve both BHBs with the HiSpID data and the standard BY choice (for spins within the BY limit). We also evolve BHBs with near-maximal spin, $\chi = 0.99$, a regime unreachable for BY initial data. Table I gives the initial data parameters of these BHB configurations.

Figure 4 shows a comparison of waveforms $r\psi_4$ extracted at an observer location $r = 75M$. We clearly see that the initial radiation content (located around $t \sim 80M$) of the BY data for equal-mass spinning BHBs with $\chi = 0.9$ has an amplitude comparable to that of the physical merger. On the other hand, the HiSpID initial data has greatly reduced initial radiation content (one order of magnitude smaller). Although not apparent in these plots, the much lower initial radiation content is not only more physical, but also leads to more accurate computations of waveforms. This initial pulse reflects from the refinement boundaries (since they are not perfectly transmissive) leading to high-frequency errors and convergence issues

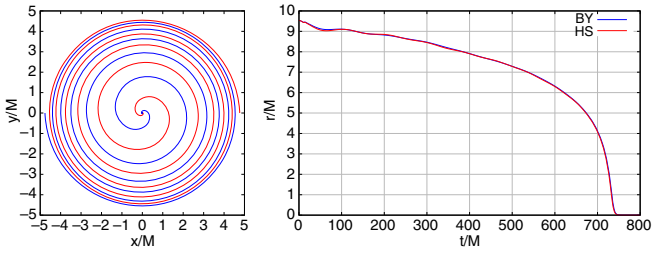

FIG. 7. The orbital trajectories of the binary and a comparative radial decay of the Lorentz boost and BY initial data. Note the near perfect agreement of the BY and HiSpID data evident in the right panel. (Left panel) The trajectories of the two black holes for HiSpID data only.

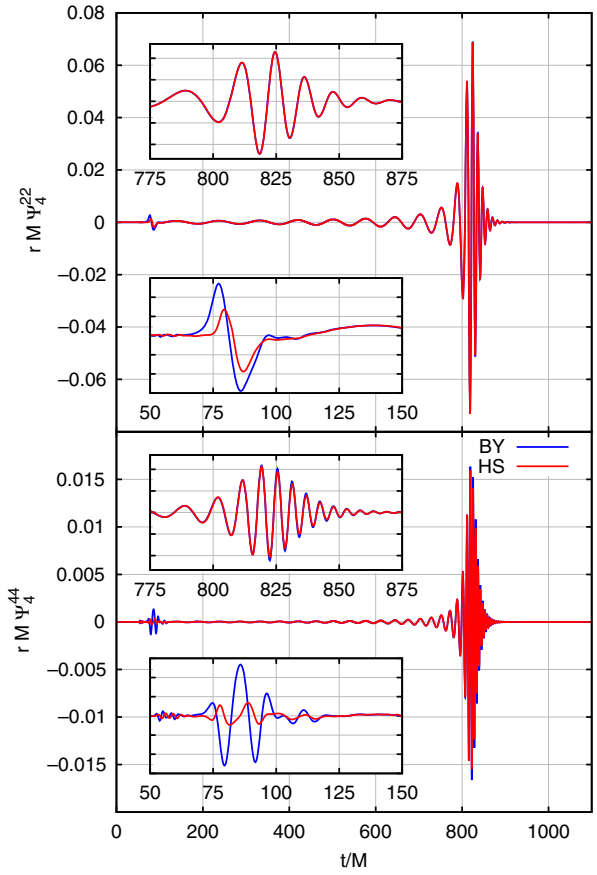

FIG. 8. Comparison of the waveforms generated from the HiSpID and BY initial data for the modes $(\ell, m) = (2, 2)$ and $(\ell, m) = (4, 4)$ for nonspinning, quasicircular binaries. Note the difference in initial radiation content at around $t = 75M$.

when looking at much finer details of the waveform phase [81,82].

The evolution of BHs with $\chi = 0.99$ requires high resolution, particularly during the first $10M$ of evolution, but otherwise proceeds with the standard moving puncture setup [4]. A summary of the properties of the final merger remnant BH are listed in Table II. Even though the initial data has no initial orbital angular momentum, UU configurations radiate angular momentum due to mutual frame dragging effects in the opposite direction, as observed in [83]. The UD configurations, on the other hand, do not radiate angular momentum, but do recoil. Here we see that both the BY and HiSpID data for black holes in a UD configuration with spins $\chi = 0.9$ lead to recoils of $35.95 \pm 0.05\ \mathrm{km\,s^{-1}}$. The much more extreme case of a UD configuration with spins $\chi = 0.99$ yields a recoil of $38.4 \pm 0.09\ \mathrm{km\,s^{-1}}$. The recoil can be modeled as [16]

$$V_{\mathrm{recoil}} = \sum_{j=1,3,5\ldots} k_j \Delta^j,$$

where $\Delta = (\chi_{(+)} - \chi_{(-)})/2$ and k_j are fitting constants (this form applies only to equal-mass binaries with vanishing total spin). With only two data points, one can only reliably fit the first constant. We find $k_1 = 39.62 \pm 0.36\ \mathrm{km\,s^{-1}}$.

In Fig. 5, we show the waveforms for the UU and UD cases for highly spinning BHs. The initial radiation content has a much smaller amplitude than the merger waveform—even in the head-on case—significantly reducing contamination of the physical signals by unresolved high-frequency reflections.

B. Quasicircular nonspinning black-hole binaries

One of the most astrophysically important applications of numerical relativity is the evolution of BHBs in quasicircular orbits. As such, it is critical that HiSpID data are able to reproduce the quasicircular binaries that can be generated by BY techniques. In this section, we will concentrate on nonspinning binaries, while in the next section, we will consider binaries with both moderate and extreme spins.

Figure 6 shows the convergence rate for a nonspinning initial data solution with the number of collocation points for a typical set of orbital parameters. Hamiltonian and momentum constraint residuals reach levels below $\mathcal{O}(10^{-6})$ near the horizon and $\mathcal{O}(10^{-10})$ in the bulk. Once again, these measures are for L^2 norms of the constraints in a small volume just outside the horizon and in the bulk of the simulation domain.

TABLE V. Initial data parameters for spinning, orbital configurations. The punctures are initially located at $(\pm b, 0, 0)$, having mass ratio $q = m_{(+)}/m_{(-)}$, with spins aligned or antialigned with the z direction, mass parameters $m_{(\pm)}$, total ADM mass M_{ADM}, and dimensionless spins χ. The linear momenta of the holes, $P^y_{(+)}$ and $P^y_{(-)}$, are initially purely in the y direction. The Bowen-York configurations are denoted by BY, and the HiSpID by HS. Finally, UU or UD denote the direction of the two spins, both either aligned (UU) or antialigned (UD).

Configuration	b/M	q	$m_{(+)}$	$m_{(-)}$	χ	$P^y_{(+)}$	$P^y_{(-)}$	M_{ADM}/M
BY80UD	5.4489	2	0.4078	0.1998	0.80	0.081882	−0.081882	0.991789
HS80UD	5.4489	2	0.6667	0.3333	0.80	0.086168	−0.083831	0.996224
HS95UU-A	4	1	0.5000	0.5000	0.95	0.103289	−0.103289	0.986854
HS95UU-B	5	1	0.5056	0.5056	0.95	0.092251	−0.092251	0.988631

In order to evaluate the effectiveness of the HiSpID approach for generating binary data, we perform a numerical evolution of a binary in the merger regime and compare our Lorentz boost data with the traditional BY solution. We chose initial parameters with low eccentricity for each set of data, as given by Table III. The BHs orbit nearly five times before merging (see Fig. 7), and at $t \sim 700M$, merge to a spinning remnant BH with the properties given in Table IV. Note the near perfect agreement of the orbital decay between the BY and HiSpID data evident in the right panel of Fig. 7.

Of course, the primary output from these simulations is the gravitational waveform. Figure 8 shows the ($\ell = 2$, $m = 2$) and ($\ell = 4$, $m = 4$) modes of ψ_4 for the HiSpID and BY binaries. While the two waveforms superpose for most of the simulation, they differ substantially in the initial bursts (located at around $t = 75M$). The BY data have nearly a factor of 2 larger amplitude for the initial burst relative to the HiSpID data for the leading (2,2) mode, and this ratio grows for the (4,4) mode to a factor ~5. This burst of initial radiation may have consequences in the cases when high accuracy of the waveforms is needed (in particular on the phase at late times) as it generates errors reflecting on the refinement boundaries of the grid [81]. Because the initial burst is much smaller, the HiSpID data have the added benefit that the initial burst does not affect the subsequent dynamics of the binary to the extent it does for BY. Hence the input parameters (BH mass and momentum) matching more closely with the actual parameters of the binary after the initial burst dissipates. We also note that there is a phase and amplitude mismatch among HiSpID and BY waveforms at merger. This may be due to a combination of slightly different initial orbital parameters and the above mentioned disparity in the initial radiation content.

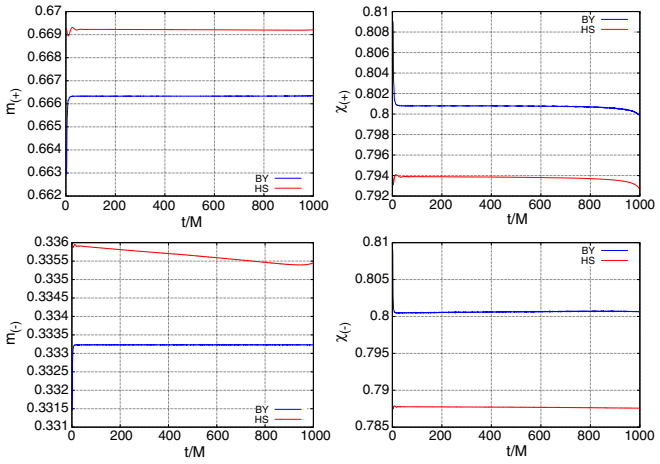

FIG. 9. The evolution of the irreducible mass and dimensionless spin of the individual black holes with $q = 2$ and $\chi = 0.8$, comparing Lorentz-boosted Kerr and Bowen-York initial data. The top panels show the larger black hole, and the bottom panels show the smaller black hole.

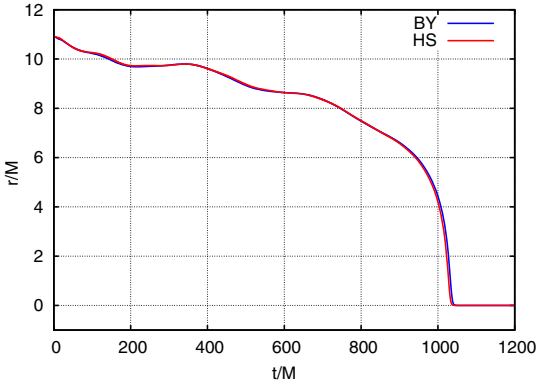

FIG. 10. The evolution of the coordinate separation between the black holes in an orbiting binary with $q = 2$ and $\chi = 0.8$, comparing Lorentz-boosted Kerr and Bowen-York initial data.

C. Quasicircular spinning black-hole binaries

To assess how accurately the HiSpID approach produces spinning binaries, we again compare evolutions of HiSpID and BY data. Here, we study a few test cases of unequal-mass black-hole-binary configurations starting in quasicircular orbits with antiparallel (UD) spins, perpendicular to the line joining the black holes. We evolve both black-hole binaries with the HiSpID data and the standard BY choice (for spins within the BY limit).

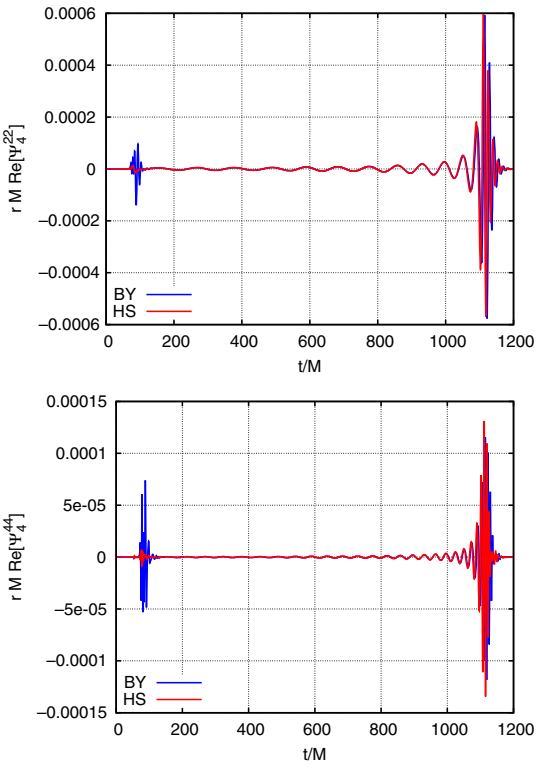

FIG. 11. Comparison of the waveforms generated from the Lorentz-boosted Kerr and Bowen-York initial data for the modes $(\ell, m) = (2, 2)$ and $(\ell, m) = (4, 4)$. Note the difference in initial radiation content at around $t = 75M$.

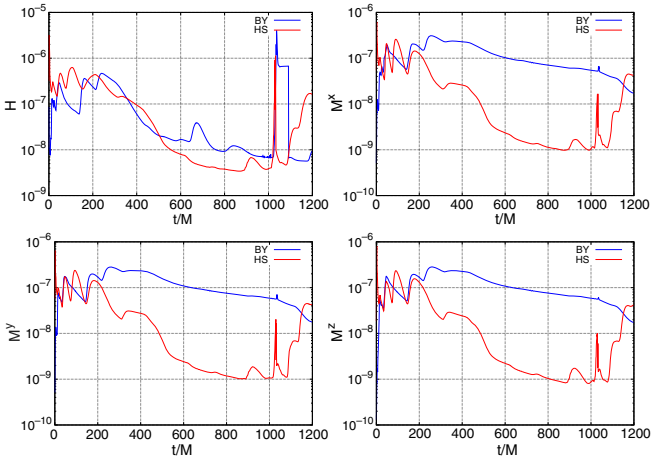

FIG. 12. The evolution of the Hamiltonian (H) and momentum (M^x, M^y, and M^z) constraints for a black-hole binary with $q = 2$ and $\chi = 0.8$, comparing Lorentz-boosted Kerr and Bowen-York initial data.

We also evolve black-hole binaries with nearly extremal parallel (UU) spins, $\chi = 0.95$, a regime unreachable for BY initial data. Table V gives the initial data parameters of these black-hole-binary configurations. Antiparallel spins result in antisymmetric emission of gravitational radiation, leading to a recoil in the merger remnant.

For given binary separations, the HiSpID and BY parameters (spin, momentum, horizon masses) are not identical, as shown in Fig. 9, since the initial radiation content and distortions are not the same. However, they are close enough for comparisons of physical quantities such as the puncture separations shown in Fig. 10 and the gravitational waveforms shown in Fig. 11. Figure 12 shows that the conformally curved initial data yield better evolved constraint satisfaction than the conformally flat case. The final measured parameters are shown in Table VI.

One of our main motivations to study a new set of initial data is to be able to simulate highly spinning black holes, beyond the BY (or conformally flat) limit, $\chi \approx 0.93$ [31,32,52]. In Fig. 13 we show the level of satisfaction of the constraints for our new initial data for spinning black-hole binaries with equal masses and spin parameters $\chi = 0.95$. The L^2 norm of the constraints converge to a level of $\mathcal{O}(10^{-7}) - \mathcal{O}(10^{-6})$ near the horizons, and down to $\mathcal{O}(10^{-10})$ in the bulk. We do not consider points interior to the horizons in our L^2 calculations. If one requires greater satisfaction of the constraints, one can fine-tune the attenuation functions to that end.

It is important to note that the actual metric functions generated by solving Eq. (26) converge even faster than the constraints themselves. In Fig. 14, we show how the function u converges with the number of collocation points. To do this, we compare the u generated with $N = 256$ collocation points with the values obtained using fewer collocation points. We do this both along the x axis (where the black holes are located) and along the y axis (in between the holes). In both cases, we find exponential convergence.

In Figs. 15 and 16, we compare the ($\ell = 2, m = 2$) mode of ψ_4 for the two UU95 runs with the corresponding SXS waveform from the SXS catalog [55]. For most of the waveform, we observe relative errors (compared to SXS) of 2% for the amplitude of the waveform. The phase differences between the two HiSpID runs and the SXS run are between 0.1 and 0.2 rad for most of the waveform. The HS95UU-A configuration agrees with the SXS simulation to a higher degree, with a phase difference of under 0.2 rad through merger.

An evolution of the mass and spin parameters for an equal-mass binary with $\chi = 0.95$ is shown in Fig. 17. The initial and final parameters for this run are listed in the final rows of Tables V and VI, respectively. To check the validity of these results, we compare the final mass and spin, calculated during the numerical simulation using the apparent horizon and isolated horizon formalism, to an analytic fitting formula (the last three columns in Table VI [18]). These analytic fitting formulas were developed using a set of 37 aligned and antialigned spinning unequal-mass systems, as well as an additional 38 simulations from the SXS catalog [55], which included aligned systems with spins up to $\chi = 0.98$. The fitting formulas give $M_{\rm rem}/M = 0.8940$ and $\chi_{\rm rem} = 0.9403$ for case A, and $M_{\rm rem}/M = 0.8933$ and $\chi_{\rm rem} = 0.9415$ for case B, differing from our measured results by about 0.01% to 0.09%. We also compare the remnant values with the SXS#157 run which falls right in between our A and B runs.

The HiSpID data using LES coordinates is not limited to $\chi \leq 0.95$. To demonstrate this, we solved the initial data for a quasicircular binary with spins $\chi = 0.974$ and a separation of $d = 10M$. As shown in Fig. 18, the constraints

TABLE VI. The relaxed mass ratio and initial spins and final remnant mass, spin, and recoil velocity. The final two columns give the analytic fits for the final mass and spin given the initial parameters.

Configuration	$q^{\rm relax}$	$\chi_1^{\rm relax}$	$\chi_2^{\rm relax}$	$M_{\rm rem}/M$	$\chi_{\rm rem}$	V [km s^{-1}]	$M_{\rm rem}^{\rm fit}/M$	$\chi_{\rm rem}^{\rm fit}$	$V^{\rm fit}$
BY80UD	0.50010	0.80053	−0.80080	0.96831	0.41037	420 ± 2	0.96844	0.40941	421.86
HS80UD	0.50185	0.78776	−0.79389	0.96815	0.41008	414 ± 7	0.96833	0.41258	419.08
HS95UU-A	1.00000	0.9465	0.9465	0.8942	0.9402	0	0.8940	0.9403	0
SXS#157	1.00000	0.9496	0.9496	0.8937	0.9409	0	0.8936	0.9410	0
HS95UU-B	1.00000	0.9520	0.9520	0.8925	0.9413	0	0.8933	0.9415	0

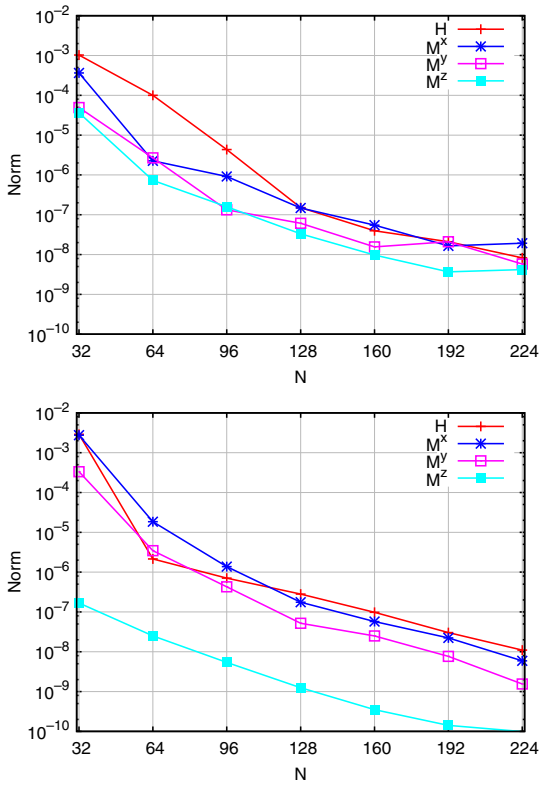

FIG. 13. Convergence of the Hamiltonian and momentum constraint residuals on the full numerical grid with an increasing number of collocation points. This example shows an equal-mass Kerr black-hole binary in a quasicircular orbit with spin $\chi = 0.95$, momentum $P^y_{(\pm)} = \pm 0.09225$, and separation $d = 10M$ using the LES coordinates. (Top panel) For a small grid along the x axis ($4.75 \leq x \leq 5.25$, $0.1 \leq y \leq 0.6$, and $0.5 \leq z \leq 1.0$). (Bottom panel) For the full numerical evolution grid.

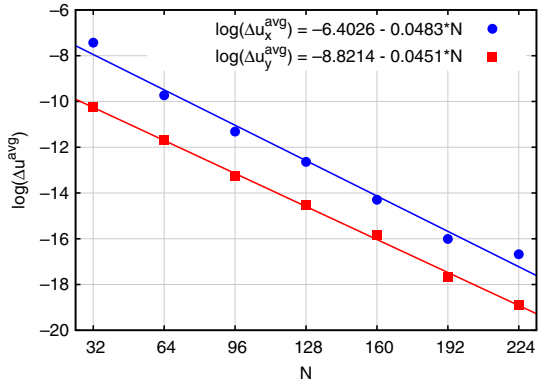

FIG. 14. Exponential convergence for the same data in Fig. 13 along the x and y axes of the averaged quantity [see Eq. (21)] $\Delta u = u_{256} - u_N$, where N is the number of collocation points. The average is taken over $0M$ to $50M$ along x or y. Since there is higher resolution near the BHs, these averages are weighted more towards the regions around the BHs. The solid lines show a best least-squares fit assuming exponential convergence.

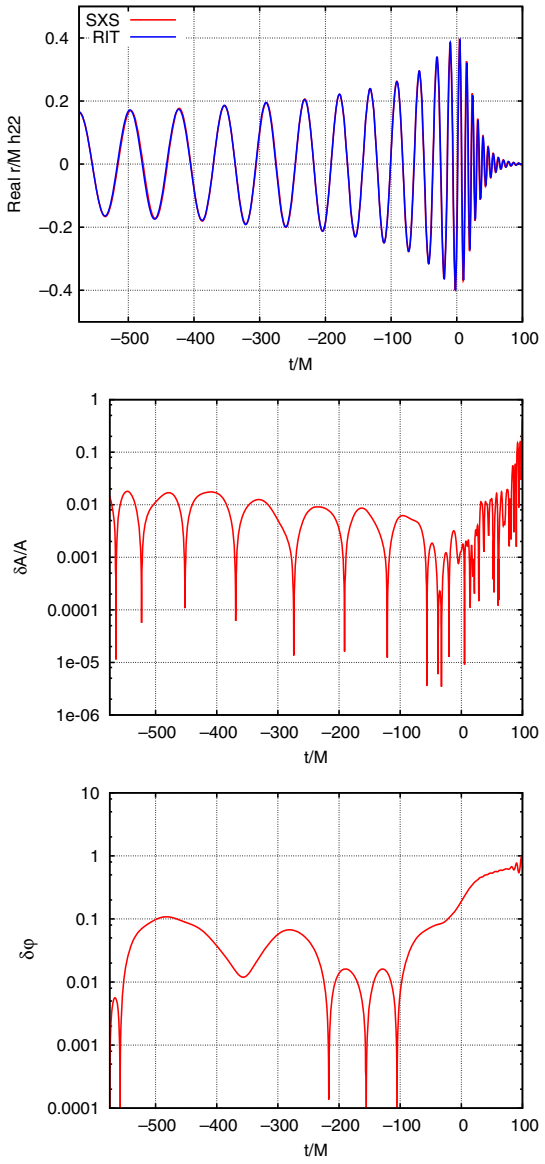

FIG. 15. The (2,2) mode of the gravitational waveform generated by an equal-mass, equal-spin (with spins $\chi = 0.95$) BHB (HS95UU-A) generated using isotropic coordinates compared to SXS catalog #157. (Middle and bottom panels) The percent difference between the two for the amplitude and phase, respectively.

converge to $\mathcal{O}(10^{-10})$ (the Hamiltonian is larger by a factor of 100, but it is still converging essentially exponentially).

To summarize, in this section we have shown that we are able to implement puncture initial data for highly spinning, orbiting black-hole binaries by attenuated superposition of conformal Lorentz-boosted Kerr metrics. We modified the TwoPunctures thorn, in the CACTUS/EinsteinToolkit framework, to solve the Hamiltonian and momentum constraint equations simultaneously for highly spinning black holes. We verified the validity of the data by showing convergence of the Hamiltonian and momentum constraint residuals with the number of collocation points in the spectral solver.

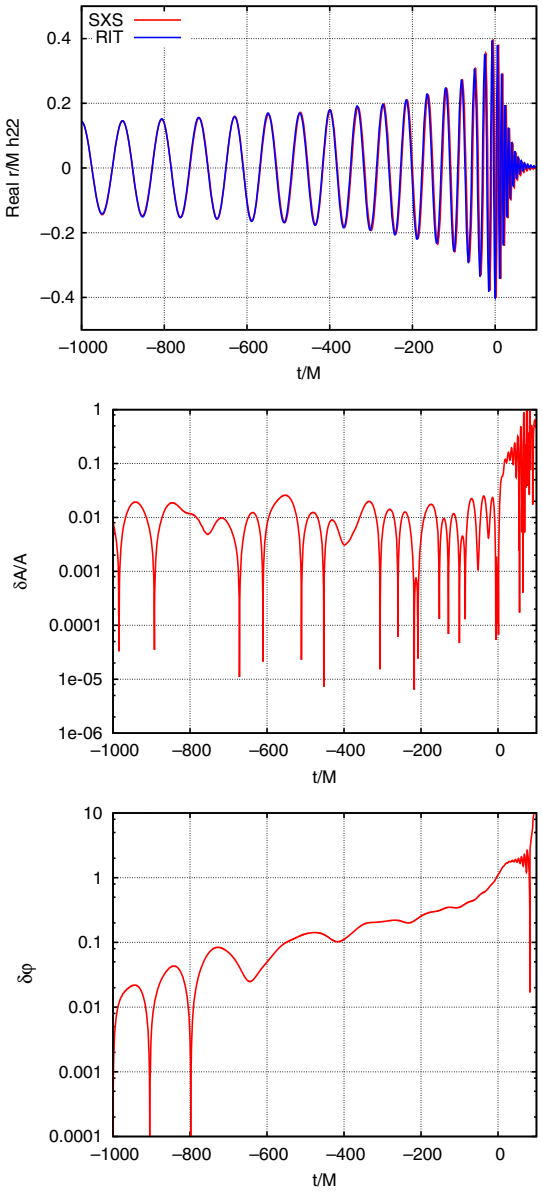

FIG. 16. The (2,2) mode of the gravitational waveform generated by equal-mass, equal spins of 0.95 BHB (HS95UU-B) generated using LES coordinates compared to SXS catalog #157. (Middle and bottom panels) The percent difference between the two for the amplitude and phase, respectively.

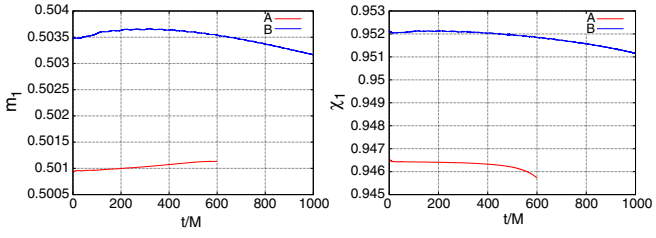

FIG. 17. The evolution of the horizon mass and the dimensionless spin of one of the individual black holes with $q = 1$ and $\chi = 0.95$.

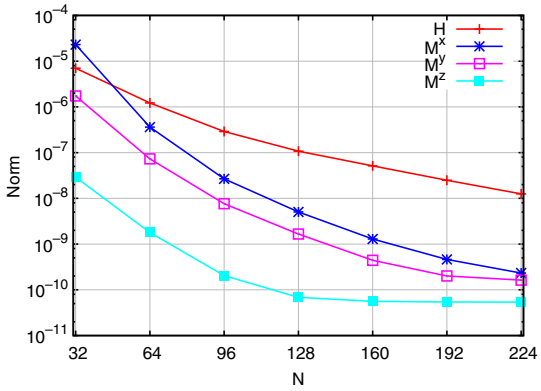

FIG. 18. Convergence of the residuals of the Hamiltonian and momentum constraints versus the number of collocation points N for a quasicircular binary in LES coordinates with $\chi = 0.974$ in the UU configuration.

We then showed, by evolving this data, that the radiation content of these initial data was much lower than the standard conformally flat choice at spins $\chi = 0.8$. This produced a more accurate and realistic computation of gravitational radiation waveforms. We go on to simulate a black-hole binary on quasicircular orbit with $\chi = 0.95$, beyond the Bowen-York limit. The mass and spin of the resulting remnant black hole agrees with the analytic fitting function estimates to between 0.01% and 0.09%.

V. CONCLUSIONS AND DISCUSSION

In this paper we were able to implement puncture initial data for highly spinning and highly boosted BHBs by the attenuated superposition of conformal Kerr and Lorentz-boosted Schwarzschild metrics and for the boosted Kerr case. We verified the validity of the data by showing convergence of the Hamiltonian and momentum constraint residuals with the number of collocation points in the spectral solver. We then showed, by evolving this data, that the spurious radiation content of these initial data was much lower than the standard conformally flat choice. This produced a more accurate and realistic computation of gravitational radiation waveforms that we compare with both, the Bowen-York initial data evolution for lower spins ($\chi = 0.90$) and the SXS's waveforms for higher spins with $\chi = 0.95$. This represents the first moving puncture evolution of highly spinning black holes beyond the conformally flat ansatz limit [32] of $\chi = 0.935$. These cleaner initial data allowed us to explore different choices of the moving puncture gauge (initial lapse and shift) in Appendix A, as well as alternative/additional evolution variables as introduced by CCZ4 [84].

This initial data implementation will allow for simulation of extremely boosted and highly spinning orbiting BHBs to explore the corners of the BHB parameter space, in a regime of theoretical and astrophysical interest. The high boost case was recently used in [53] to study the head-on

high-energy collision of nonspinning black holes. It also allows for revisiting some of the most interesting spin dynamic effects in BHBs, such as the hang-up [11], flip-flops [12,85,86], and large recoils [18,87], as well as extreme BHB collisions [53].

ACKNOWLEDGMENTS

The authors thank M. Campanelli, G. Lovelace, and M. Zilhão for the discussions. The authors gratefully acknowledge the NSF for financial support from Grants No. PHY-1607520, No. AST-1516150, No. ACI-1516125, No. PHY-1305730, No. PHY-1212426, No. PHY-1229173, No. AST-1028087, No. OCI-0725070 (PRAC Subcontract No. 2077-01077-26), No. OCI-0832606, and No. ACI-1550436. Computational resources were provided by XSEDE allocation TG-PHY060027N, and by NewHorizons and BlueSky Clusters at Rochester Institute of Technology, which were supported by NSF Grants No. PHY-0722703, No. DMS-0820923, No. AST-1028087, and No. PHY-1229173. This work was supported in part by the 2013–2014 Astrophysical Sciences and Technology Graduate Student Fellowship, funded in part by the New York Space Grant Consortium, administered by Cornell University.

APPENDIX A: GAUGE CONDITIONS

The original moving puncture breakthrough formulation [4] remains widely used, and produces reliable BHB evolutions, as well as multi-BH systems [26]. It also functions in the presence of matter, as in neutron-star mergers [88–90]. The choice of the gauges, i.e., Eq. (29a) plays a crucial role in stabilizing the numerical evolutions. There is still a range of possibilities for choosing the specific form of the gauges. While preserving the numerical stability properties one would like to improve the accuracy of the simulation for a given resolution and grid structure.

Some questions about the accuracy and convergence of the moving puncture method have been raised in [81]. Recently, Etienne *et al.* [82] studied how modifications to the lapse evolution can ameliorate the numerical errors that lead to poor waveform convergence.

Here we study other choices for the initial lapse and its time evolution to control and improve the accuracy of the numerical results for highly spinning BHs and relativistic collisions of BHs generating large amplitude gauge waves.

The Bona-Massò gauge condition for the lapse evolution is [91]

$$(\partial_t - \beta^i \partial_i)\alpha = -\alpha^2 f(\alpha) K, \tag{A1}$$

where in the original moving puncture approach $f(\alpha) = 2/\alpha$. We also consider $f(\alpha) = 1/\alpha$, with gauge speed equal to 1, and $f(\alpha) = 8/(3\alpha(3-\alpha))$, with approximate shock avoiding properties [56].

For the initial lapse we use either $\alpha(t=0) = 1/\psi_{\rm BL}^2$ [4] or $\alpha(t=0) = 2/(1+\psi_{\rm full}^4)$ [11], which behave like $\sim r^2$ and $\sim r^4$, respectively, near the puncture, and have the form of the Schwarzschild lapse in isotropic coordinates at large r. Here, $\psi_{\rm full} = [\det(\gamma_{ij})]^{1/12}$. In addition, we investigate the form $\alpha(t=0) = 1/(2\psi_{\rm BL} - 1)$. This goes like $\sim r$ near the puncture, similar to the "trumpetlike" behavior observed at later evolution times when gauges settle down to a quasistationary behavior [92], while conserving the form of the Schwarzschild lapse in isotropic coordinates at asymptotically large r.

1. Highly spinning black holes

Notably, the simple choice of the initial lapse $\alpha_0 = 1/(2\psi_{\rm BL} - 1)$ has advantages over the other choices studied for the entire evolution by providing increased accuracy and computational efficiency. Here, we display the results of the evolutions from rest of BHBs with intrinsic spin $\chi = 0.99$. Figure 19 shows that we can achieve comparably accurate results with many fewer grid points. The curves follow closely to each other, but with the new lapse we use 80 points per dimension compared to the 125 needed with the original initial lapse. This provides a speedup factor of $(125/80)^4 \sim 6$.

The improvement of the new initial lapse also translates into a more accurate description of the final remnant BH, as shown in Fig. 20. Note that even at lower resolutions we observe a similar gain.

We interpret these results as indicating that a better choice of the initial lapse leads to a better coordinate evolution. The intensities of the initial gauge waves are reduced, thus allowing a better distribution of grid points, resulting in a more efficient numerical computation. See for instance the horizon coordinate radius evolution in Figs. 19 and 20.

Figure 21 displays the effects of the initial lapse on the waveform. We see the notable reduction of the unphysical oscillations premerger while reproducing accurately the physical merger waveform for the dominant modes $(\ell, m) = (2, 0)$ and $(\ell, m) = (2, 2)$. Note that this reduction of the errors due to improved gauge choices is in addition to and independent from the reduction of the initial burst of radiation (with respect to the BY data) that has a physical content, despite being an undesirable effect.

Figures 19, 20, and 21 show three different resolutions for the waveforms and horizon quantities for the highly spinning $\chi = 0.99$ case. The convergence order was calculated for each of these quantities. For the individual BH spin, irreducible mass, horizon mass, and dimensionless spin, we find average convergence orders of 7.6, 6.2, 8.2, and 8.2, respectively. The eighth-order convergence is expected if the errors are dominated by the spatial finite difference stencil. The same quantities for the final remnant BH have convergence orders between 3.3 and 4.3.

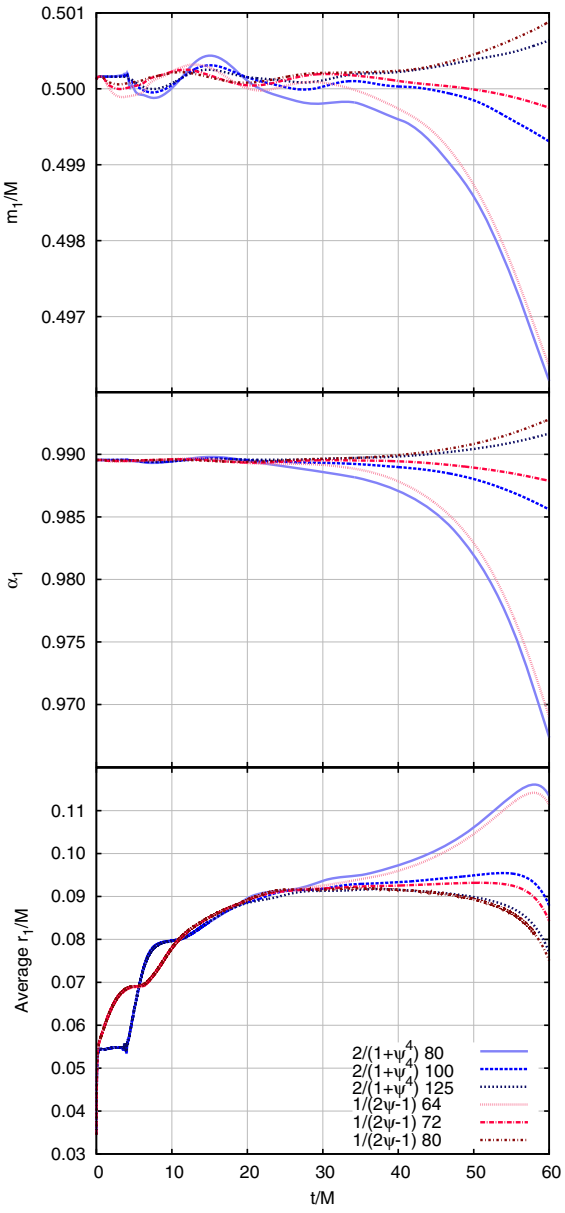

FIG. 19. The effects of the choice of the initial lapse on the individual BH masses (top panel), spins (middle panel), and coordinate radii (bottom panel). The benefits of the new initial lapse are evident since they follow the higher resolution behavior with many fewer grid points by $(80/125)^3$. For all runs $f(\alpha) = 2/\alpha$.

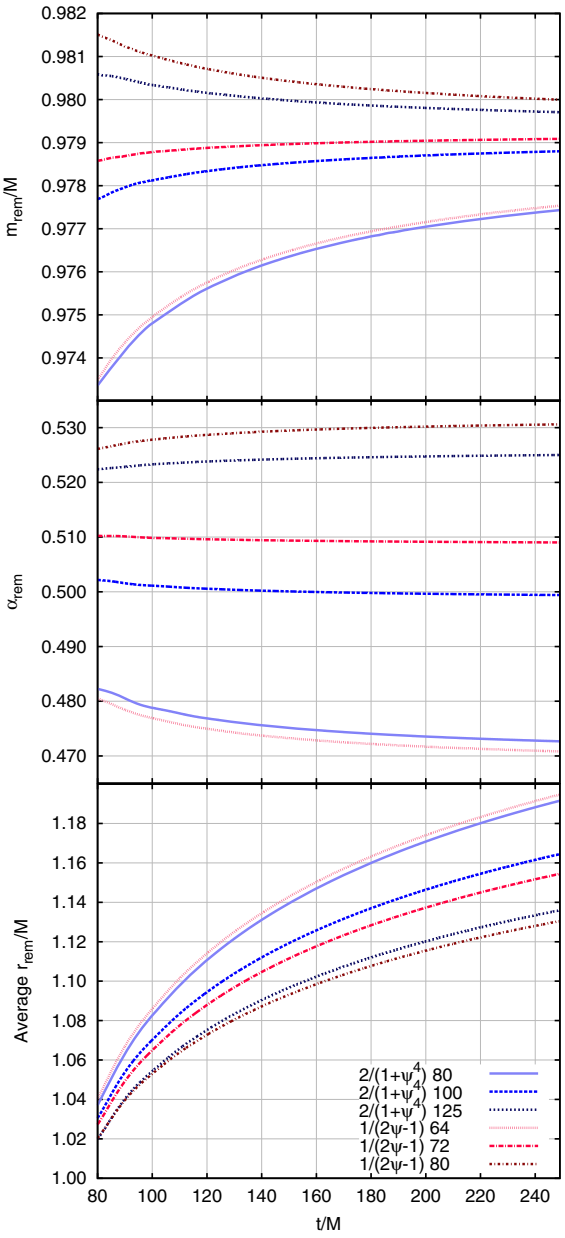

FIG. 20. The effects of the choice of the initial lapse on the final BH mass (top panel), spin (middle panel), and coordinate radius (bottom panel). The benefits of the new initial lapse are evident since they follow the higher resolution behavior with many fewer grid points. For all runs $f(\alpha) = 2/\alpha$.

We expect a fourth-order convergence if the errors are dominated by the time integration. For the amplitude and phase of the (2,2) mode, we find a convergence order between 3 and 4 after the BHs merge. This is consistent with the time integration errors.

2. Quasicircular orbits

Here, we study the effects of lapse evolution choices on the case study of equal-mass, nonspinning, orbiting BHBs. The Lorentz boost initial data has a lower radiation content than the boosted BY data and allows us to see more clearly the effects of the initial choice and evolution of the lapse. In this section, all runs studied are at the medium resolution, labeled "100" in Figs. 19–21.

Figure 22 displays the effects of gauge versus resolution on physical quantities like the horizon mass (left column) and horizon radius (right column). We expect the horizon mass to be essentially conserved during the orbital period up to merger. We can see that this physical observable varies very little with different gauge choices. On the other

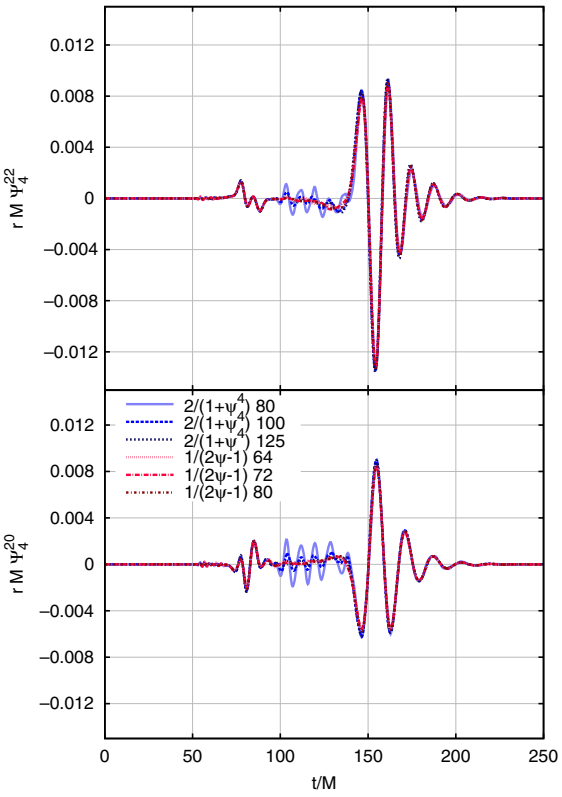

FIG. 21. The effects of the choice of the initial lapse on the waveforms. The benefits of the new initial lapse are evident since they show much less initial noise before the merger.

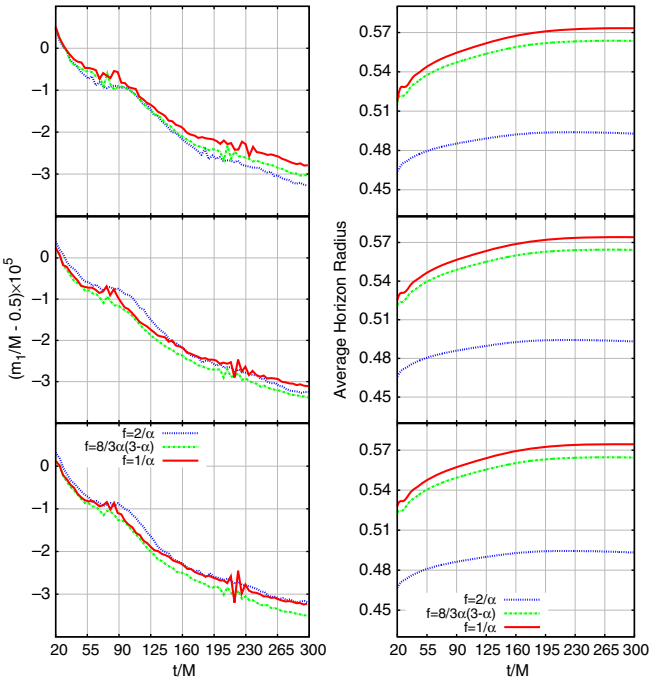

FIG. 22. Individual BH horizon masses (left column) and coordinate radii of the horizons (right column) versus time for different evolution functions $f(\alpha)$ for the lapse. Initial lapse $\alpha_0 = 2/(1+\psi^4_{\rm full})$ (top row), $\alpha_0 = 1/\psi^2_{\rm BL}$ (middle row), $\alpha_0 = 1/(2\psi_{\rm BL}-1)$ (bottom row).

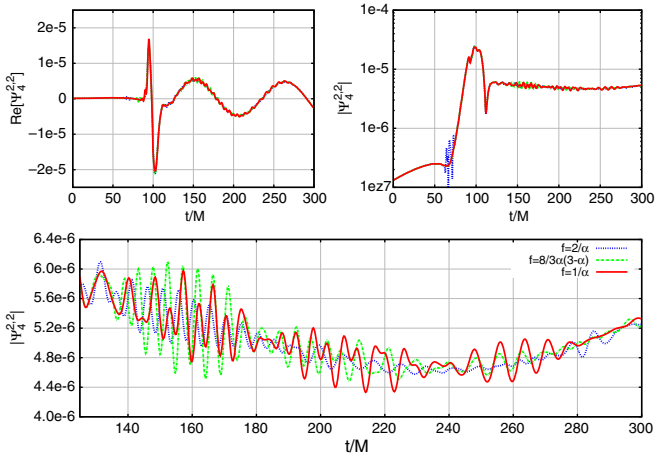

FIG. 23. Waveforms extracted at an observer location $r = 90M$. Real part of Ψ_4 (upper left panel) and the amplitude of those waveforms (upper right panel). (Lower panel) Enlargement of the amplitude oscillations for different evolution functions $f(\alpha)$ for the lapse. The initial lapse here is $\alpha_0 = 2/(1+\psi^4_{\rm BL})$.

hand, we observe that the coordinate radius varies with the evolution of the lapse choice, but not as much with the initial lapse. After a sudden growth, typical of a gauge settling, the horizon radius reaches a constant value. The original moving puncture choice, $f(\alpha) = 2/\alpha$, keeps the value of the horizon coordinate closer to its original value, which could be beneficial for setting up the initial mesh refinement levels.

Figure 23 displays the waveform as seen by an observer at $r = 90M$ from the sources for different evolution functions $f(\alpha)$ for the lapse. The initial lapse here is $\alpha_0 = 2/(1+\psi^4_{\rm full})$. While physical quantities like the

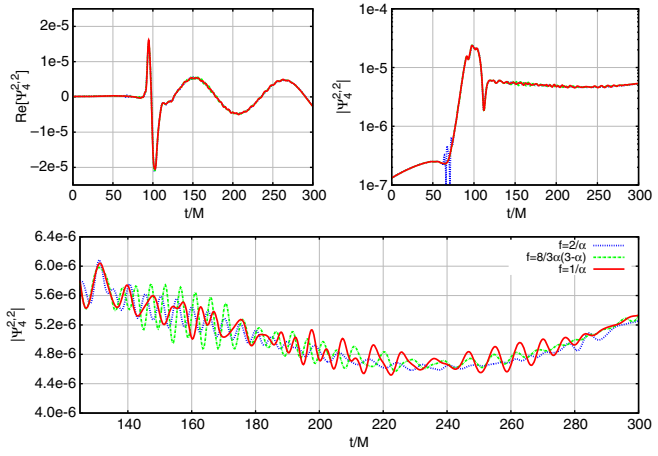

FIG. 24. Waveforms extracted at an observer location $r = 90M$. Real part of Ψ_4 (upper left panel) and the amplitude of those waveforms (upper right panel). The bottom panel shows an enlargement of the amplitude oscillations for different evolution functions $f(\alpha)$ for the lapse. The initial lapse implemented here is $\alpha_0 = 1/\psi^2_{\rm BL}$.

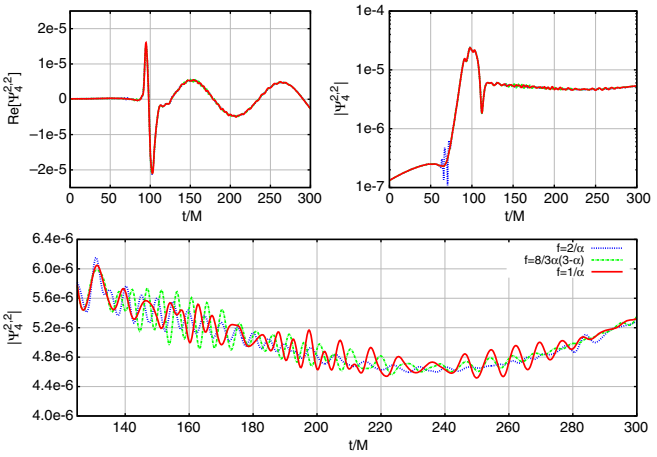

FIG. 25. Waveforms extracted at an observer location $r = 90M$. Real part of Ψ_4 (upper left panel) and the amplitude of those waveforms (upper right panel). (Lower panel) Enlargement of the amplitude oscillations for different evolution functions $f(\alpha)$ for the lapse. The initial lapse here is $\alpha_0 = 1/(2\psi_{\rm BL} - 1)$.

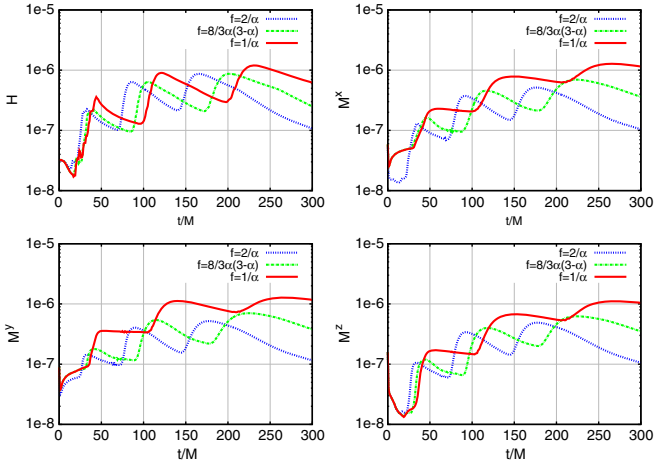

FIG. 27. L^2-norms of the violations of the Hamiltonian and three components of the momentum constraints versus time for different evolution functions $f(\alpha)$ for the lapse. The initial lapse here is $\alpha_0 = 1/\psi^2_{\rm BL}$.

waveform and its amplitude are essentially independent of the gauge choices, numerical errors, which produce the high-frequency noise, are not. The bottom panel of the figure shows a close-up view of the amplitude during the postinitial pulse period. We observe that overall the choice $f(\alpha) = 2/\alpha$ produces a lower amplitude of this high-frequency noise.

Figures 24 and 25 display a similar behavior for the waveforms, but their close-up view of the noise shows a smaller amplitude, which suggests that the choice of the initial lapse $\alpha_0 = 1/\psi^2_{\rm BL}$ or $\alpha_0 = 1/(2\psi_{\rm BL} - 1)$ leads to smaller amplitude gauge waves.

Since the moving puncture approach is a free evolution of the general relativistic field equations, a very important method to monitor its accuracy is to verify the satisfaction of the Hamiltonian and momentum constraints. We also monitor the BSSN constraints, which are on the order of 10^{-7} throughout the duration of the evolution.

Figures 26–28 display the L^2 norm of the nonvanishing values of the Hamiltonian and momentum components of the constraints. We observe that the propagation of errors travel at different speeds, associated with the gauge velocities $\sqrt{2}$, $\sqrt{4/3}$, and 1 for $f(\alpha) = 2/\alpha$, $8/(3\alpha(3-\alpha))$, and $1/\alpha$, respectively. We also observe slightly larger violations for the choice $f(\alpha) = 1/\alpha$, and $\alpha_0 = 2/(1 + \psi^4_{\rm BL})$.

We thus conclude that while all three evolution choices for the lapse are viable to evolve typical BHB simulations, the original moving puncture choice $f(\alpha) = 2/\alpha$ and the initial lapse $\alpha_0 = 1/\psi^2_{\rm BL}$ or $\alpha_0 = 1/(2\psi_{\rm BL} - 1)$ are

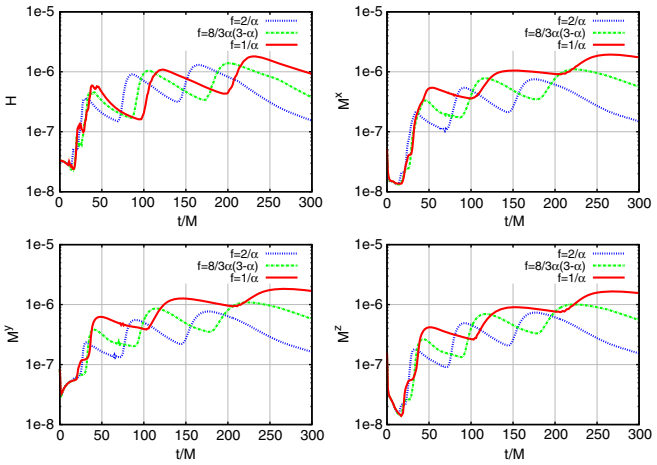

FIG. 26. L^2-norms of the violations of the Hamiltonian and three components of the momentum constraints versus time for different evolution functions $f(\alpha)$ for the lapse. The initial lapse here is $\alpha_0 = 2/(1 + \psi^4_{\rm full})$.

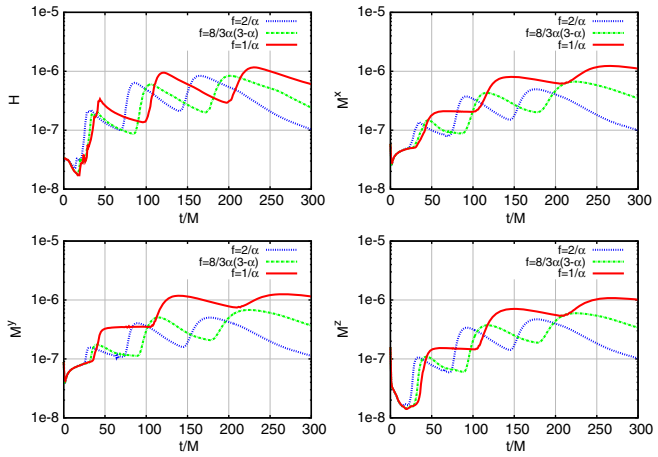

FIG. 28. L^2-norms of the violations of the Hamiltonian and three components of the momentum constraints versus time for different evolution functions $f(\alpha)$ for the lapse. The initial lapse here is $\alpha_0 = 1/(2\psi_{\rm BL} - 1)$.

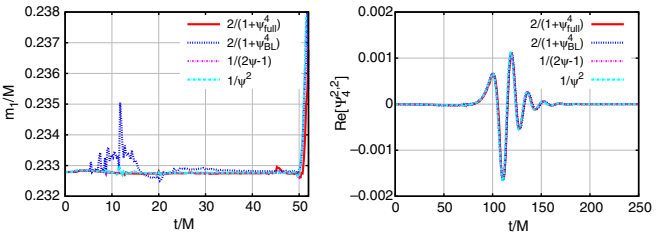

FIG. 29. Horizon mass of the boosted BH with $P_x/m_{\rm H} = \pm 2$ and waveform after collision for different choices of the initial lapse and evolution $f(\alpha) = 2/\alpha$.

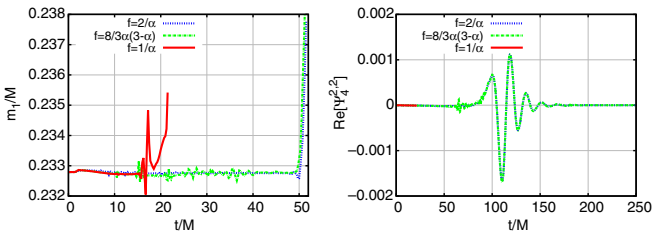

FIG. 31. Horizon mass (left panel) of the boosted BH with $P_x/m_{\rm H} = \pm 2$ and waveform (right panel) after collision for the initial lapse $\alpha_0 = 1/(2\psi_{\rm BL} - 1)$ and different choices of the evolution of the lapse.

somewhat preferred. This study suggests there might be even more optimal choices of α_0 and $f(\alpha)$, as well as shift evolution gauge conditions. We also note that in the independent study of Ref. [82], a higher gauge velocity is preferred for the early stage of evolution.

3. Relativistic head-on collisions

Since we observe a notable benefit on using the initial lapse $\alpha_0 = 1/(2\psi_{\rm BL} - 1)$ in evolutions of highly spinning BHs, we would like to explore their effect on another extreme configuration: high-energy relativistic collisions of BHs. The collisions were studied in Refs. [93–96] with regard to potential applications to collider-generated mini BHs. Here we will consider them as a test case for comparing different gauge conditions.

In Fig. 29 we use physical observables such as the individual horizon masses and the gravitational radiation waveforms as indicators of the numerical accuracy of the evolutions. We observe that the initial lapse $\alpha_0 = 1/(2\psi_{\rm BL} - 1)$ gives the best behavior for the horizons mass (i.e., the most constant) and a waveform with reduced noise.

The preferred behavior of the initial lapse $\alpha_0 = 1/(2\psi_{\rm BL} - 1)$ is also confirmed with regard to the constraint preservation as shown in Fig. 30, closely followed by the choice $\alpha_0 = 1/\psi^2_{\rm full}$.

In these evolutions we have taken the standard choice for the moving puncture evolution of the lapse, $f(\alpha) = 2/\alpha$ in Eq. (A1). It is also worthwhile to explore alternative evolutions of $f(\alpha) = 1/\alpha$, with gauge speed equal to 1, and $f(\alpha) = 8/(3\alpha(3-\alpha))$, with approximate shock avoiding properties [56]. The results of such evolutions are displayed in Figs. 31 and 32, where we have taken an initial separation of the binary $d = 66M$, $P_x/m_{\rm H} = \pm 2$, and used the initial lapse $\alpha_0 = 1/(2\psi_{\rm BL} - 1)$.

We first observe that the results of Figs. 31 and 32 indicate that with our numerical setup the evolution $f(\alpha) = 1/\alpha$ fails to complete (i.e., crashes) generating large errors, while the form $f(\alpha) = 8/(3\alpha(3-\alpha))$ is stable, but less accurate than the standard $f(\alpha) = 2/\alpha$.

However, we find that for larger initial $P/m_{\rm H}$ values, the lapse evolution equation characterized by $f(\alpha) = 2/\alpha$ fails to complete the evolution while the (approximate) shock avoiding form $f(\alpha) = 8/(3\alpha(3-\alpha))$ always succeeds. In these cases, a large amplitude gauge wave is generated by the high-energy collision initial data which

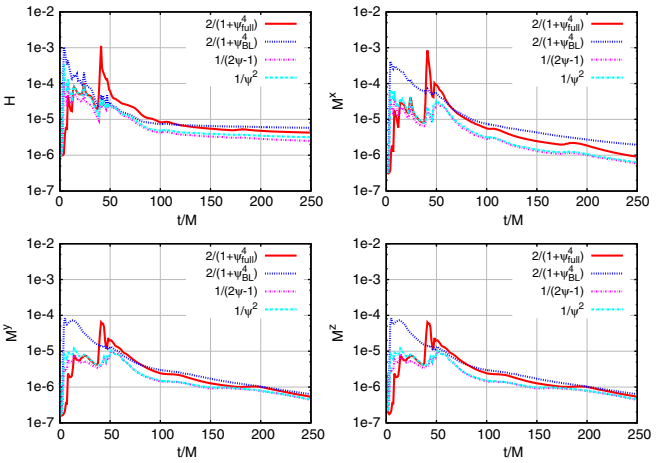

FIG. 30. Hamiltonian and momentum constraints during the free evolution for different choices of the initial lapse and evolution $f(\alpha) = 2/\alpha$.

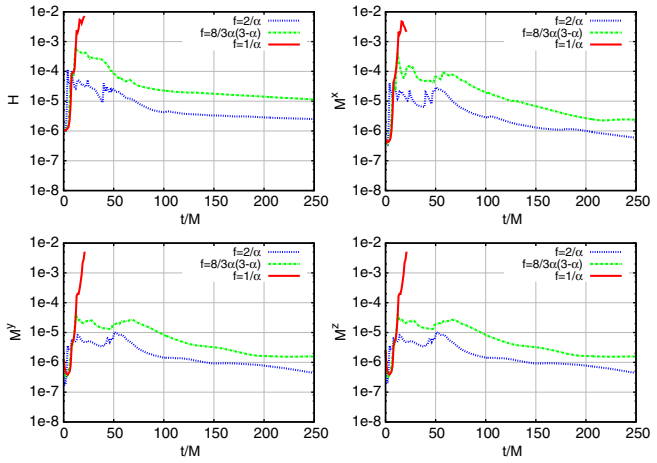

FIG. 32. Hamiltonian (H) and momentum (M^x, M^y, and M^z) constraints during the free evolution for the initial lapse $\alpha_0 = 1/(2\psi_{\rm BL} - 1)$ and different choices of the evolution of the lapse.

leads to an inability for the numerics to resolve the waves and stabilize the system. While one can try to fine-tune parameters of the evolution or change the evolution equations (for instance to a Z4 type [84]) the form $f(\alpha) = 8/(3\alpha(3-\alpha))$ represents a valid alternative to the standard $f(\alpha) = 2/\alpha$ evolution (which can still be used by starting collisions further apart or slightly grazing).

APPENDIX B: CALCULATING THE ADM ENERGY, MOMENTUM, AND SPIN

For the sake of completeness we give here the explicit form of the ADM mass and the linear and angular momenta used in the identification of the initial data parameters.

In an asymptotically flat spacetime, in asymptotically Cartesian coordinates, the ADM mass is given by [97]

$$E[h_{ab}] = \frac{1}{16\pi}\lim_{r\to\infty}\sum_{a,b=1}^{3}\oint (h_{ab,a} - h_{aa,b})\frac{x^b}{r}r^2 \mathrm{d}\Omega,$$

where $h_{ab} = \delta_{ab} + c_{ab}(\theta,\phi)/r + \mathcal{O}(1/r^2)$ is the 3-metric, $x^a = (x,y,z)$ are Cartesian coordinates (at spatial infinity), and (r,θ,ϕ) are the usual spherical coordinates. The integral is over an $r = \text{const}$ sphere, and $\mathrm{d}\Omega = \sin\theta \mathrm{d}\theta \mathrm{d}\phi$. Only the $\mathcal{O}(1/r)$ terms in the metric contribute to the ADM mass.

For the case of superimposed boosted Schwarzschild BHs, we have

$$h_{ab} = \left(1 + \frac{m_{(+)}}{2r_{(+)}} + \frac{m_{(-)}}{2r_{(-)}} + u\right)^4 (\tilde{S}^{(+)}_{ab} + \tilde{S}^{(-)}_{ab} - \delta_{ab}),$$

where

$$\left(1 + \frac{m_{(+)}}{2r_{(+)}}\right)^4 \tilde{S}^{(+)}_{ab} = S^{(+)}_{ab},$$
$$\left(1 + \frac{m_{(-)}}{2r_{(-)}}\right)^4 \tilde{S}^{(-)}_{ab} = S^{(-)}_{ab},$$

$m_{(\pm)}$ are the mass parameters of the two Schwarzschild BHs, $r_{(\pm)}$ are $\mathcal{O}(r)$ with angular dependence, and $S^{(\pm)}_{ab}$ indicates Schwarzschild metrics in boosted coordinates. Since $\tilde{S}_{ab} = \delta_{ab} + \mathcal{O}(1/r)$, the ADM mass takes the form

$$\begin{aligned} E[h_{ab}] &= E[\psi^4 \tilde{S}^{(+)}_{ab}] + E[\psi^4 \tilde{S}^{(-)}_{ab}] - E[\psi^4 \delta_{ab}] \\ &= E\left[\left(1 + \frac{2m_{(+)}}{r_{(+)}}\right)\tilde{S}^{(+)}_{ab}\right] + E\left[\left(1 + \frac{2m_{(-)}}{r_{(-)}}\right)\tilde{S}^{(-)}_{ab}\right] \\ &\quad + E\left[\left(\frac{2m_{(-)}}{r_{(-)}} + \frac{4\hat{u}}{r}\right)\delta_{ab}\right] + E\left[\left(\frac{2m_{(+)}}{r_{(+)}} + \frac{4\hat{u}}{r}\right)\delta_{ab}\right] \\ &\quad - E\left[\left(\frac{2m_{(+)}}{r_{(+)}} + \frac{2m_{(-)}}{r_{(-)}} + \frac{4\hat{u}}{r}\right)\delta_{ab}\right] \\ &= \gamma_{(+)}m_{(+)} + \gamma_{(-)}m_{(-)} + E\left[\frac{4\hat{u}}{r}\delta_{ab}\right], \end{aligned} \tag{B1}$$

where $u = \hat{u}(\theta,\phi)/r + \mathcal{O}(1/r^2)$. The first two terms of Eq. (B1) are the ADM masses of boosted Schwarzschild BHs and are thus equal to $\gamma_{(+)}m_{(+)}$ and $\gamma_{(-)}m_{(-)}$, respectively. Finally, $E[4\hat{u}/r\delta_{ab}] = \frac{1}{8\pi}\oint \hat{u}\mathrm{d}\Omega$.

The ADM momentum is given by

$$P_a[K_{ab}] = \frac{1}{8\pi}\lim_{r\to\infty}\sum_{b=1}^{3}\oint (K_{ab} - \delta_{ab}K)\frac{x^b}{r}r^2\mathrm{d}\Omega,$$

with $K = \sum_{a=1}^{3} K^a{}_a$. Using Eqs. (3), (4), (23), (22), and (24) in the asymptotic region, the integrand becomes

$$K_{ab} - \delta_{ab}K = K^{(+)}_{ab} - \delta_{ab}K_{(+)} + K^{(-)}_{ab} - \delta_{ab}K_{(-)} + (\tilde{\mathbb{L}}b)_{ab},$$

where $K^{(\pm)}_{ab}$ indicates the extrinsic curvature tensors for isolated BHs. Given the momentum parameters $P^{(\pm)}_a$, the corresponding ADM momentum for an isolated BH is $P_a[K^{(\pm)}_{ab}] = P^{(\pm)}_a$. Therefore, using the linearity of the integral, the ADM momentum for a BHB is

$$\begin{aligned} P_a[K_{ab}] &= P_a[K^{(+)}_{ab}] + P_a[K^{(-)}_{ab}] + P_a[(\tilde{\mathbb{L}}b)_{ab}] \\ &= P^{(+)}_a + P^{(-)}_a + P_a[(\tilde{\mathbb{L}}b)_{ab}]. \end{aligned}$$

The ADM angular momentum is given by the first moment of the ADM momentum:

$$J^a[K_{ab}] = \frac{\epsilon^{abc}}{8\pi}\lim_{r\to\infty}\sum_{b,c,d=1}^{3}\oint x_b(K_{cd} - \delta_{cd}K)\frac{x^d}{r}r^2\mathrm{d}\Omega.$$

Using the same linearity and asymptotic properties, we can write this as

$$J^a[K_{ab}] = J^a_{(+)} + J^a_{(-)} + J^a[(\tilde{\mathbb{L}}b)_{ab}].$$

[1] B. Abbott *et al.* (Virgo and LIGO Scientific Collaborations), Phys. Rev. Lett. **116**, 061102 (2016).
[2] B. P. Abbott *et al.* (Virgo and LIGO Scientific Collaborations), Phys. Rev. Lett. **116**, 241103 (2016).
[3] F. Pretorius, Phys. Rev. Lett. **95**, 121101 (2005).
[4] M. Campanelli, C. O. Lousto, P. Marronetti, and Y. Zlochower, Phys. Rev. Lett. **96**, 111101 (2006).
[5] J. G. Baker, J. Centrella, D.-I. Choi, M. Koppitz, and J. van Meter, Phys. Rev. Lett. **96**, 111102 (2006).
[6] B. P. Abbott *et al.* (Virgo and LIGO Scientific Collaborations), Phys. Rev. Lett. **116**, 221101 (2016).
[7] B. P. Abbott *et al.* (Virgo and LIGO Scientific Collaborations), Phys. Rev. X **6**, 041015 (2016).
[8] G. Lovelace *et al.*, Classical Quantum Gravity **33**, 244002 (2016).
[9] B. P. Abbott *et al.* (Virgo and LIGO Scientific Collaborations), Phys. Rev. D **94**, 064035 (2016).
[10] C. S. Reynolds, Classical Quantum Gravity **30**, 244004 (2013).
[11] M. Campanelli, C. O. Lousto, and Y. Zlochower, Phys. Rev. D **74**, 041501(R) (2006).
[12] C. O. Lousto and J. Healy, Phys. Rev. Lett. **114**, 141101 (2015).
[13] M. Campanelli, C. O. Lousto, Y. Zlochower, and D. Merritt, Astrophys. J. **659**, L5 (2007).
[14] M. Campanelli, C. O. Lousto, Y. Zlochower, and D. Merritt, Phys. Rev. Lett. **98**, 231102 (2007).
[15] C. O. Lousto, Y. Zlochower, M. Dotti, and M. Volonteri, Phys. Rev. D **85**, 084015 (2012).
[16] C. O. Lousto and Y. Zlochower, Phys. Rev. D **87**, 084027 (2013).
[17] D. A. Hemberger, G. Lovelace, T. J. Loredo, L. E. Kidder, M. A. Scheel, B. Szilágyi, N. W. Taylor, and S. A. Teukolsky, Phys. Rev. D **88**, 064014 (2013).
[18] J. Healy, C. O. Lousto, and Y. Zlochower, Phys. Rev. D **90**, 104004 (2014).
[19] J. Aasi *et al.* (LIGO Scientific, Virgo, and NINJA-2 Collaborations), Classical Quantum Gravity **31**, 115004 (2014).
[20] B. Aylott *et al.*, Classical Quantum Gravity **26**, 114008 (2009).
[21] B. Aylott *et al.*, Classical Quantum Gravity **26**, 165008 (2009).
[22] P. Ajith *et al.*, Classical Quantum Gravity **29**, 124001 (2012).
[23] I. Hinder *et al.*, Classical Quantum Gravity **31**, 025012 (2014).
[24] C. O. Lousto and Y. Zlochower, Phys. Rev. Lett. **106**, 041101 (2011).
[25] C. O. Lousto and Y. Zlochower, Phys. Rev. D **88**, 024001 (2013).
[26] C. O. Lousto and Y. Zlochower, Phys. Rev. D **77**, 024034 (2008).
[27] M. Shibata and K. Uryu, Phys. Rev. D **74**, 121503 (2006).
[28] L. Baiotti and L. Rezzolla, Phys. Rev. Lett. **97**, 141101 (2006).
[29] J. M. Bowen and J. W. York, Jr., Phys. Rev. D **21**, 2047 (1980).
[30] G. B. Cook and J. W. York, Jr., Phys. Rev. D **41**, 1077 (1990).
[31] S. Dain, C. O. Lousto, and R. Takahashi, Phys. Rev. D **65**, 104038 (2002).
[32] C. O. Lousto, H. Nakano, Y. Zlochower, B. C. Mundim, and M. Campanelli, Phys. Rev. D **85**, 124013 (2012).
[33] S. Dain, Phys. Rev. Lett. **87**, 121102 (2001).
[34] J. W. York, Jr., Phys. Rev. Lett. **82**, 1350 (1999).
[35] G. B. Cook, Living Rev. Relativ. **3**, 5 (2000).
[36] H. P. Pfeiffer and J. W. York, Jr., Phys. Rev. D **67**, 044022 (2003).
[37] G. Lovelace, M. Boyle, M. A. Scheel, and B. Szilagyi, Classical Quantum Gravity **29**, 045003 (2012).
[38] G. Lovelace, M. A. Scheel, R. Owen, M. Giesler, R. Katebi, B. Szilágyi, T. Chu, N. Demos, D. A. Hemberger, L. E. Kidder, H. P. Pfeiffer, and N. Afshari, Classical Quantum Gravity **32**, 065007 (2015).
[39] M. A. Scheel, M. Giesler, D. A. Hemberger, G. Lovelace, K. Kuper, M. Boyle, B. Szilágyi, and L. E. Kidder, Classical Quantum Gravity **32**, 105009 (2015).
[40] M. Hannam, S. Husa, B. Bruegmann, J. A. Gonzalez, and U. Sperhake, Classical Quantum Gravity **24**, S15 (2007).
[41] F. Löffler, J. Faber, E. Bentivegna, T. Bode, P. Diener, R. Haas, I. Hinder, B. C. Mundim, C. D. Ott, E. Schnetter, G. Allen, M. Campanelli, and P. Laguna, Classical Quantum Gravity **29**, 115001 (2012).
[42] EinsteinToolkit home page: http://einsteintoolkit.org.
[43] CACTUS Computational Toolkit home page: http://cactuscode.org.
[44] E. Schnetter, S. H. Hawley, and I. Hawke, Classical Quantum Gravity **21**, 1465 (2004).
[45] P. Marronetti, M. Huq, P. Laguna, L. Lehner, R. A. Matzner, and D. Shoemaker, Phys. Rev. D **62**, 024017 (2000).
[46] E. Bonning, P. Marronetti, D. Neilsen, and R. Matzner, Phys. Rev. D **68**, 044019 (2003).
[47] M. Ansorg, B. Brügmann, and W. Tichy, Phys. Rev. D **70**, 064011 (2004).
[48] W. Tichy, B. Brügmann, M. Campanelli, and P. Diener, Phys. Rev. D **67**, 064008 (2003).
[49] B. J. Kelly, W. Tichy, M. Campanelli, and B. F. Whiting, Phys. Rev. D **76**, 024008 (2007).
[50] B. J. Kelly, W. Tichy, Y. Zlochower, M. Campanelli, and B. F. Whiting, Classical Quantum Gravity **27**, 114005 (2010).
[51] B. C. Mundim, B. J. Kelly, Y. Zlochower, H. Nakano, and M. Campanelli, Classical Quantum Gravity **28**, 134003 (2011).
[52] G. Cook and J. W. York, Jr., Phys. Rev. D **41**, 1077 (1990).
[53] J. Healy, I. Ruchlin, C. O. Lousto, and Y. Zlochower, Phys. Rev. D **94**, 104020 (2016).
[54] A. H. Mroue, M. A. Scheel, B. Szilagyi, H. P. Pfeiffer, M. Boyle *et al.*, Phys. Rev. Lett. **111**, 241104 (2013).
[55] See http://www.black-holes.org/waveforms.
[56] M. Alcubierre, Classical Quantum Gravity **20**, 607 (2003).
[57] R. Arnowitt, S. Deser, and C. W. Misner, in *Gravitation: An Introduction to Current Research*, edited by L. Witten (John Wiley, New York, 1962), p. 227.
[58] M. Alcubierre, *Introduction to 3+1 Numerical Relativity* (Oxford University Press, New York, 2008).
[59] S. Brandt and B. Brügmann, Phys. Rev. Lett. **78**, 3606 (1997).
[60] S. R. Brandt and E. Seidel, Phys. Rev. D **54**, 1403 (1996).
[61] W. Krivan and R. H. Price, Phys. Rev. D **58**, 104003 (1998).

[62] J. G. Baker, M. Campanelli, and C. O. Lousto, Phys. Rev. D **65**, 044001 (2002).
[63] Y. Zlochower, J. G. Baker, M. Campanelli, and C. O. Lousto, Phys. Rev. D **72**, 024021 (2005).
[64] M. Zilhão and S. C. Noble, Classical Quantum Gravity **31**, 065013 (2014).
[65] Y. T. Liu, Z. B. Etienne, and S. L. Shapiro, Phys. Rev. D **80**, 121503 (2009).
[66] See http://www.holoborodko.com/pavel/mpfr/.
[67] See http://www.mpfr.org/.
[68] H. P. Pfeiffer, G. B. Cook, and S. A. Teukolsky, Phys. Rev. D **66**, 024047 (2002).
[69] D. Brown, O. Sarbach, E. Schnetter, M. Tiglio, P. Diener, I. Hawke, and D. Pollney, Phys. Rev. D **76**, 081503 (2007).
[70] D. Brown, P. Diener, O. Sarbach, E. Schnetter, and M. Tiglio, Phys. Rev. D **79**, 044023 (2009).
[71] G. Lovelace, Ph.D. thesis, California Institute of Technology, 2007.
[72] P. Grandclement, S. Bonazzola, E. Gourgoulhon, and J. A. Marck, J. Comput. Phys. **170**, 231 (2001).
[73] P. Marronetti, W. Tichy, B. Brügmann, J. Gonzalez, and U. Sperhake, Phys. Rev. D **77**, 064010 (2008).
[74] J. Thornburg, Classical Quantum Gravity **21**, 743 (2004).
[75] O. Dreyer, B. Krishnan, D. Shoemaker, and E. Schnetter, Phys. Rev. D **67**, 024018 (2003).
[76] J. Winicour, in *General Relativity and Gravitation, Volume 2*, edited by A. Held (Plenum, New York, 1980), p. 71.
[77] M. Campanelli and C. O. Lousto, Phys. Rev. D **59**, 124022 (1999).
[78] C. O. Lousto and Y. Zlochower, Phys. Rev. D **76**, 041502(R) (2007).
[79] M. Alcubierre, B. Brügmann, P. Diener, M. Koppitz, D. Pollney, E. Seidel, and R. Takahashi, Phys. Rev. D **67**, 084023 (2003).
[80] J. R. van Meter, J. G. Baker, M. Koppitz, and D.-I. Choi, Phys. Rev. D **73**, 124011 (2006).
[81] Y. Zlochower, M. Ponce, and C. O. Lousto, Phys. Rev. D **86**, 104056 (2012).
[82] Z. B. Etienne, J. G. Baker, V. Paschalidis, B. J. Kelly, and S. L. Shapiro, Phys. Rev. D **90**, 064032 (2014).
[83] M. Campanelli, C. O. Lousto, and Y. Zlochower, Phys. Rev. D **74**, 084023 (2006).
[84] D. Alic, C. Bona-Casas, C. Bona, L. Rezzolla, and C. Palenzuela, Phys. Rev. D **85**, 064040 (2012).
[85] C. O. Lousto, J. Healy, and H. Nakano, Phys. Rev. D **93**, 044031 (2016).
[86] C. O. Lousto and J. Healy, Phys. Rev. D **93**, 124074 (2016).
[87] C. O. Lousto and Y. Zlochower, Phys. Rev. Lett. **107**, 231102 (2011).
[88] M. Anderson, E W. Hirschmann, L. Lehner, S. L. Liebling, P M. Motl, D. Neilsen, C. Palenzuela, and J. E. Tohline, Phys. Rev. D **77**, 024006 (2008).
[89] L. Baiotti, B. Giacomazzo, and L. Rezzolla, Phys. Rev. D **78**, 084033 (2008).
[90] K. Kiuchi, Y. Sekiguchi, M. Shibata, and K. Taniguchi, Phys. Rev. D **80**, 064037 (2009).
[91] C. Bona, J. Massó, E. Seidel, and J. Stela, Phys. Rev. Lett. **75**, 600 (1995).
[92] B. Brügmann, Gen. Relativ. Gravit. **41**, 2131 (2009).
[93] U. Sperhake, V. Cardoso, F. Pretorius, E. Berti, and J. A. Gonzalez, Phys. Rev. Lett. **101**, 161101 (2008).
[94] M. Shibata, H. Okawa, and T. Yamamoto, Phys. Rev. D **78**, 101501 (2008).
[95] U. Sperhake, V. Cardoso, F. Pretorius, E. Berti, T. Hinderer, and N. Yunes, Phys. Rev. Lett. **103**, 131102 (2009).
[96] U. Sperhake, E. Berti, V. Cardoso, and F. Pretorius, Phys. Rev. Lett. **111**, 041101 (2013).
[97] R. M. Wald, *General Relativity* (University of Chicago Press, Chicago, 1984).